Perforated Dielectric Transmitarray Lens for Ka Band Applications

Xiuquan Zhang

996922399

Abstract

This report presents a novel design of lightweight, compact and highly directional lens antennas for automotive radar application at Ka band. Two lenses were developed using a single layer of dielectric sheet with different perforation schemes to achieve required gradient index of refraction for beam collimation. Both perforated dielectric lenses cover an area of 15cm×15cm, and are divided into triangular lattices (or equivalently rhombic unit cells). Air holes with either variable diameters or depths with sub-wavelength spacing are used to allow continuous tuning of the phase of transmitted signal over 360^o range at 34.3GHz. Both lenses are capable of converting an omni-directional wavefront into a planar wavefront, and vice versa. The transmission and reflection coefficients versus hole diameters and depths are calculated using finite element method of HFSS program. Both lenses are able to provide above 18 dB directivity improvement with respect to the source and smaller than 4^o of beamwidth at 34.3GHz. Some future improvements for the lenses are also discussed at the end of the report.

1. Introduction

Quite recently, lens antennas have gained much attention as research interest has expanded into the use of millimeter wave and sub-millimeter wave frequency bands. The use of dielectric lenses date back to the early days of experiments associated with the verification of the optical properties of electromagnetic waves at 60GHz [1]. However, it was not until World War II that lenses gained interest as antenna elements. Even then they were not widely used because of their bulky size at rather low frequencies. There is a renewed interest in dielectric lenses nowadays due to the availability of low loss dielectric materials and smaller lens physical sizes at millimeter wavelengths. In addition, present-day numerically controlled machines have enabled low-cost fabrication of quite sophisticated lenses made with very good tolerances.

Lens antennas are viable alternatives to the conventional curved shaped reflector antennas which have been widely used as high gain radiators in radar and communications. The gain of the reflector antenna is a function of its physical aperture area, and realizing a high gain reflector antenna will result in a heavy and bulky dish structure, which is impractical to be integrated into the bodies of the vehicles. Moreover, beam-steering capability has to be achieved through mechanical movement of the antenna, which requires a large amount of space and mechanical hardware. Beam steering capability is necessary in automotive radar applications, since the tracking and determination of the exact position of an object is essential for the most functions realized by the radar sensor. While phased arrays have good beam scanning capabilities, they require many expensive, bulky, and lossy circuit components such as phase shifters and power distribution networks which made them impractical for our application.

Various configurations of lens antennas have been developed by researchers. In [2], a 6×6 element reconfigurable transmitarray operates in C-band and uses five varactor diodes in each unit cell to control the transmission phase. In [3] and [4], a four-layer transmitarray operating at 30GHz is designed using a dual-resonant double square ring as the unit cell element. Results of a 7.5%, −1 dB gain bandwidth and 47% radiation efficiency are reported. In [5], a compact 7×7 flat lens using aperture coupled microstrip patch with tuning stubs as the phasing elements at X-band was proposed. These solutions have worked well at microwave frequencies, however since they have employed metallic layers or phasing elements in their designs, the conductor loss, excitation of surface waves and mutual coupling are expected to be more severe at millimeter and sub-millimeter frequencies. It is also more difficult to manufacture these lenses with sub-wavelength unit cells and multi-layer configuration at these frequency bands, thus alternative solutions will be needed.

There are already some alternative solutions proposed using all-dielectric lenses with no metallic components. A well-known example shown in Fig.1 is the phase-correcting

Fresnel zone plate lens [6] consists of a set of radially symmetric rings cut into the dielectric, known as Fresnel zones. The focusing is achieved by diffraction and interference, rather than refraction. It is also lighter and has lower loss than hyperboloid and spherical lenses. Another example is a dielectric zoned flat lens [7] with two layers and 16 zones shown in Fig.2. It is based on multi-dielectric material philosophy where two different dielectric slabs are stacked together and then each slab divided into set of concentric zones with different dielectric constant. A more recent design shown in Fig. 3 is a single layer slotted dielectric flat lens with 21×21 unit cells [8]. The unit cell that forming the lens is based on cutting slots having same depth in both sides of a low loss host dielectric substrate to produce phase compensation from 0^o to 360^o by controlling the width of the cut slot.

Being partly inspired by some of the previous works, this report presents a perforated dielectric lens operates at 34.3GHz for automotive radar applications. The perforations result in the change of effective permittivity of the dielectric material and provide required phase compensation at each location of the lens surface. Using only single layer of dielectric without any metallic components to construct the lens makes it a good candidate for integration with other planar devices.

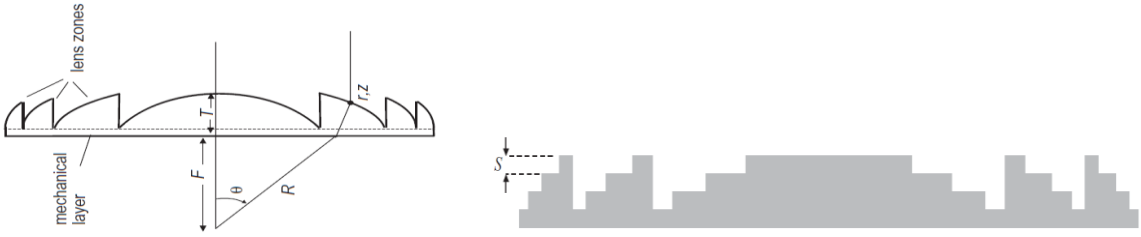

(a) (b)

Fig. 1 (a) Fresnel-zoned plate and (b) phase correcting Fresnel zone plate lens.

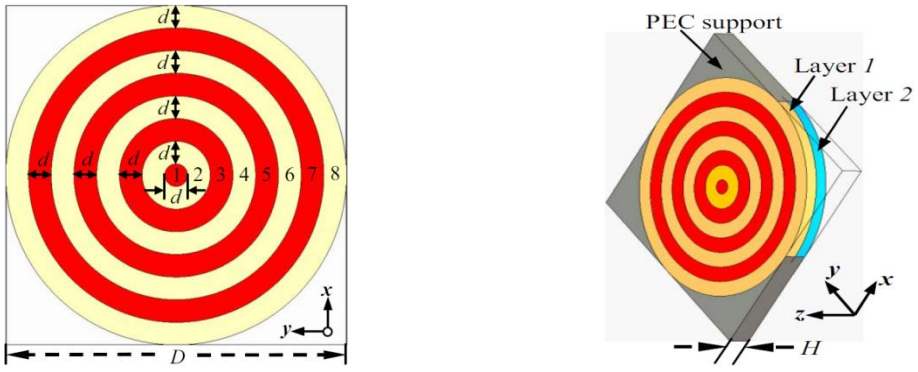

(a) (b)

Fig. 2 Zoned two-layer dielectric flat lens. (a) top view and (b) top view.

(a) (b)

Fig. 3 Inhomogeneous single layer slotted dielectric flat lens. (a) Geometry of the proposed unit cell. (b) 3D view of the lens with the feeder.

2. Principle of Operation of the Transmitarray Lens

Similar to an optical convex lens, for transmitting mode, the transmitarray transforms the spherical wave emanating from the source into a plane wave at the output. On the other hand, the transmitarray focuses the incident plane wave onto the feeding point. The lens is composed of a group of equally spaced zones (columns of holes perforated with same radius and depth in each column) working all together to correct the phase of the incoming EM wave radiated by the source with different path length as shown in Fig. 4. The required phase compensation Φ, at each location along the lens to collimate the beam can be determined by using Fermat's principle [9] as:

$$\Phi = \frac{2\pi}{\lambda_o}\left[\sqrt{r^2 + F^2} - F\right] \pm 2\pi N\,, \qquad r \in \left[0,\ \frac{D}{2}\right] \tag{1}$$

where F, D and r are the focal length, diameter, and position along the lens respectively, and λ_o is the free space wavelength. The required phase compensation at each location with different F/D on the lens is plotted using MATLAB in Fig. 5.

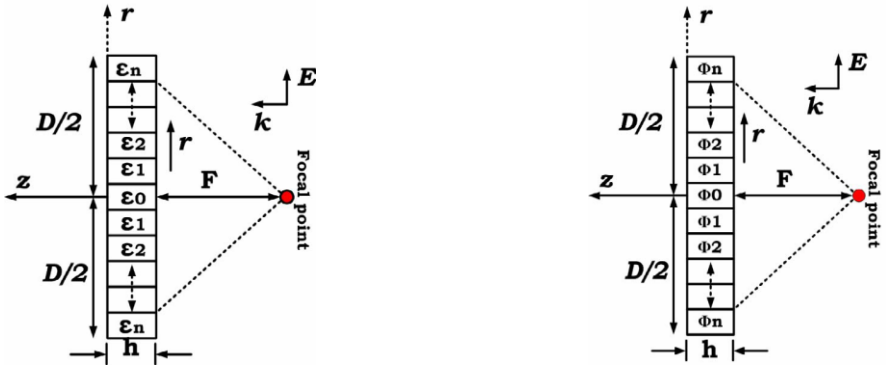

(a) (b)

Fig. 4 (a) Multidielectric and (b) phase correction design philosophy [9].

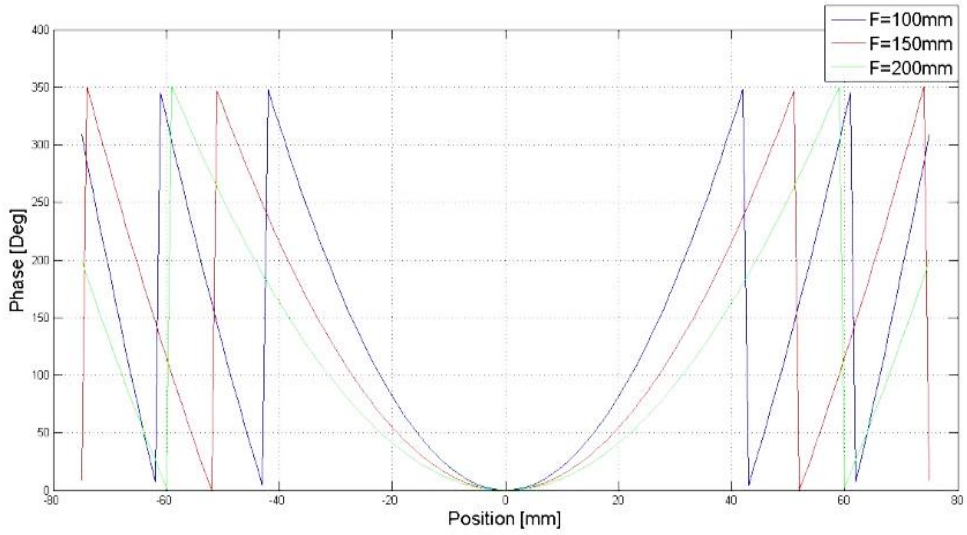

Fig. 5 Required phase at each location on the 15cm wide transmitarray lens for F = 10cm (F/D = 0.667), F = 15cm (F/D = 1), and F = 20cm (F/D = 1.333).

It can be observed that with the same width of the lens, as F/D ratio increases, the number of phase wrappings decreases. Only 350^{o} of phase compensation is required.

3. Lens Design and Simulation Results

3.1 Materials for the Lens

The choice of material for the lens is mainly based on the relative permittivity, dissipation factor, and mechanical stability. The dielectric loss factor, also known as the dissipation factor (Df) is very important at millimeter wave frequencies. It is defined from the tangent of the loss angle (tan δ), and is hence also called the loss tangent. For many materials, it tends to be proportional to frequency, so the higher the frequency, the more likely it will be to dominate overall material loss. On the other hand, the relative permittivity decreases with frequency, but in the millimeter wave region (>30GHz), the values are approximately constant. The material itself should also be strong enough to withstand perforation and installation.

The table below is a list of available substrate materials with high permittivity and low loss from Rogers Product Selector Guide [10]:

Table 1: Possible materials and properties for lens construction.

Material Name	**AD1000**	**RT/duroid 6010LM**	**TMM13i**	**RO3010**	**RO3210**
Bulk Dk	10.2	10.7	12.2	11.2	10.8
Dissipation Factor	0.0023	0.0023	0.0019	0.002	0.002
Max Available Thickness (inch)	0.12	0.1	0.5	0.05	0.05
Max Available Thickness (mm)	3.048	2.54	12.7	1.27	1.27
Isotropy	Anisotropic	Anisotropic	Isotropic	Anisotropic	Anisotropic
Min # of Layers Needed	3	3	1	6	6
Material Composition	woven glass reinforced PTFE	PTFE ceramic	hydrocarbon ceramic	PTFE ceramic	PTFE ceramic woven glass reinforced

The other high permittivity and low loss materials for millimeter wave include gallium arsenide (GaAs) with $\varepsilon_r = 13.2$, $\tan \delta = 0.001$ and magnesium titanate (Mg_2TiO_4) with $\varepsilon_r = 16.1$, $\tan \delta = 0.0002$ [11].

Most materials have some degree of anisotropy, the values for $\varepsilon_x/\varepsilon_z$ and $\varepsilon_y/\varepsilon_z$ vary from lot to lot, and the exact values are usually not available from the vendor. For example, for RO3010, the $\varepsilon_x/\varepsilon_z$ and $\varepsilon_y/\varepsilon_z$ can vary from 1.1 to 1.3 and RT/duroid 6010LM, the $\varepsilon_x/\varepsilon_z$ and $\varepsilon_y/\varepsilon_z$ can vary from 1.2 to 1.4 [12]. Also, the substrate material should have both large enough thickness and permittivity to achieve at least 360^o phase correction. Since only the substrate boards with certain thicknesses are available, bond-ply will be needed to glue multilayers together when single layer is not thick enough.

In this project, a TMM13i substrate board with thickness of 0.3 inch (7.62 mm) is used for the lens design. It has low loss, large dielectric constant, and isotropic property, and only one layer is needed for the lens design.

3.2 Unit Cell Characterization

The required phase correction at each unit cell is a function of the phase delay between the phase center of the feed and the closest interface of the lens. By locally adjusting the effective dielectric constant of the lens through perforating the substrate, phase correction of the incident wave is achieved. The effective dielectric constant is controlled by either varying the diameter or the depth of the holes: the larger the hole diameter or deeper the hole, the lower the effective permittivity for the given substrate material. This perforation can be implemented as a uniform square or triangular lattice of

holes drilled in the substrate [13], as shown in Fig. 6. If the diameter of holes (d) and the distance between holes (s) are kept below half of the guided wavelength at the frequency of operation, the substrate will appear to have a uniform effective permittivity. The effective relative permittivity ε_{eff} can be estimated using:

$$\varepsilon_{eff} = \varepsilon_r (1-\alpha) + \alpha \tag{2}$$

where for square lattice:

$$\alpha = \frac{\pi}{4}\left(\frac{d}{s}\right)^2 \tag{4}$$

and for triangular lattice:

$$\alpha = \frac{\pi}{2\sqrt{3}}\left(\frac{d}{s}\right)^2 \tag{3}$$

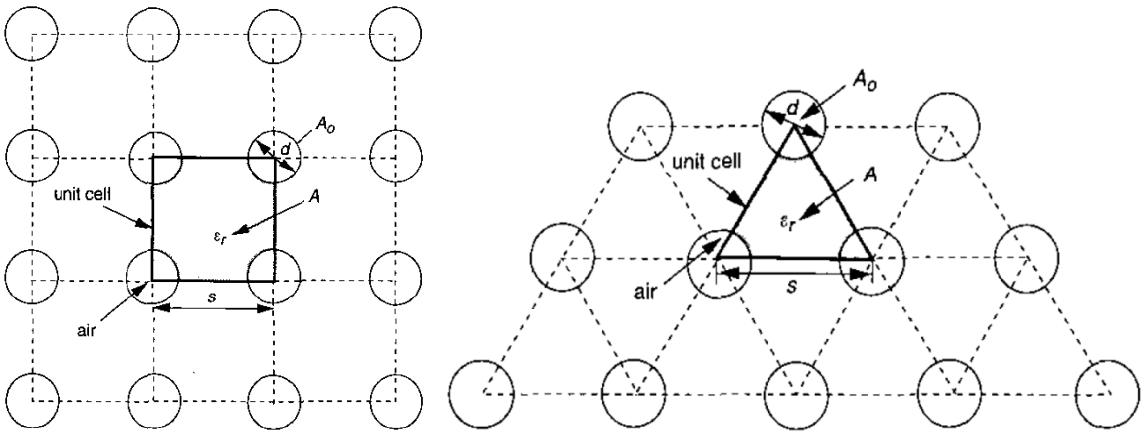

(a) (b)

Fig. 6 Perforated dielectric substrate with (a) square and (b) triangular lattice [13].

Fig. 7 below shows the filling factors for both triangular and square lattices as a function of d/s. Fig. 8 compares the effective permittivity range that can be achieved by drilling holes substrate materials with initial relative permittivity ε_r = 12.2 (TMM13i) and ε_r = 6.3 (TMM6). A higher filling factor is achieved using the triangular lattice since the holes are packed closer together than with the square lattice. The triangular lattice allows for a wider range of effective permittivity, thus it is used in this work.

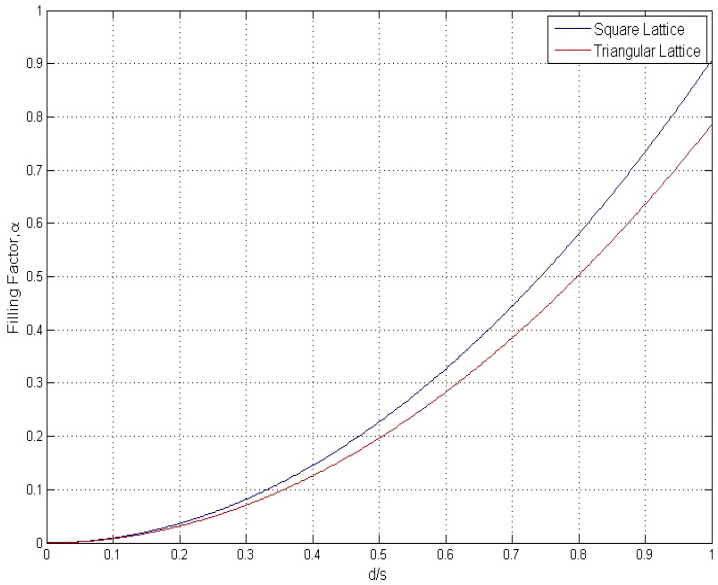

Fig. 7 Filling facror versus d/s for perforated dielectric unit cell.

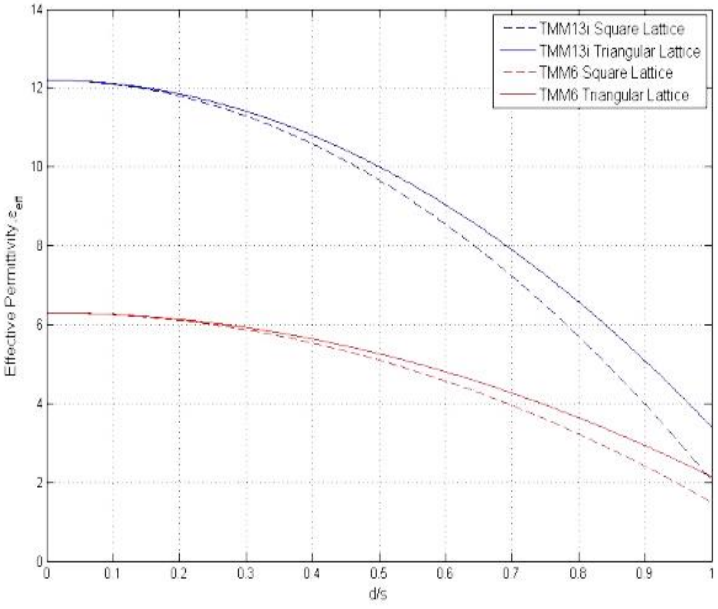

Fig. 8 Effective permittivities of the perforated dielectric materials of TMM13i and TMM6 with square and triangular lattices.

For triangular lattice of unit cells, with d = 3.4 mm, s = 4 mm, the minimum relative effective permittivity can be achieved is 4.86. The index of refraction, intrinsic impedance and phase velocity of the resultant dielectric substrate after perforation can be calculated as:

$$n = \sqrt{\mu_r \varepsilon_{eff}} = \sqrt{\varepsilon_r \left(1 - \frac{\pi}{2\sqrt{3}} \left(\frac{d}{s}\right)^2\right) + \frac{\pi}{2\sqrt{3}} \left(\frac{d}{s}\right)^2} \quad (5)$$

$$Z_{unitcell} \approx \frac{\eta_0 e^{j \tan \delta}}{\sqrt{\varepsilon_r \left(1 - \frac{\pi}{2\sqrt{3}} \left(\frac{d}{s}\right)^2\right) + \frac{\pi}{2\sqrt{3}} \left(\frac{d}{s}\right)^2}} \quad (6)$$

$$v_\varphi = \frac{c}{\sqrt{\varepsilon_{eff}}} = \frac{c}{\sqrt{\varepsilon_r \left(1 - \frac{\pi}{2\sqrt{3}} \left(\frac{d}{s}\right)^2\right) + \frac{\pi}{2\sqrt{3}} \left(\frac{d}{s}\right)^2}} \quad (7)$$

Due to the fabrication constraints of CNC milling machine, the approach described above has to be modified. It is difficult to drill through holes of diameters smaller than 0.6 mm on a 7.62 mm substrate due to limited flute length of small drill bits, two lenses of different types of perforation schemes have been developed. The type I lens has through holes of diameters ranging from 0.6mm to 3.4mm, and the through holes of diameters below 0.6mm are replaced with blind holes by varying the hole depth to create required effective permittivity. The type II lens has only blind holes with fixed diameter of 3.4 mm, but the hole depth is varied from 0 to 7.6mm. Fig. 9 below shows the through hole versus blind hole, drilling blind holes with the same diameter will have lower fabrication cost since only one drill bit is required.

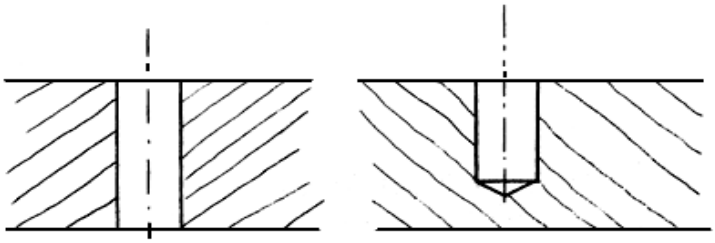

Fig. 9 Left: through hole, right: blind hole.

Two configurations of unit cells are proposed and shown in Fig. 10. Both unit cells of the transmitarray are enclosed in a rhombic air-box with side length of 4 mm, and substrate thickness of 7.62 mm. Each cell has four circular holes of equal diameters centered at each corner. Master and slave boundary conditions are applied to each pair of the side walls and Floquet ports are applied to the top and bottom walls of the air-box with TM mode of excitation. In this manner, the unit cells are repeated to infinity in the simulator. This approach assumes quasi-periodic condition where the lens dimension is much larger than the unit cell, and hole diameters and depths of neighbouring cells have only very small variation. However in reality, the lens can never be infinite in extent and effects such as edge diffraction are not accounted in the simulation.

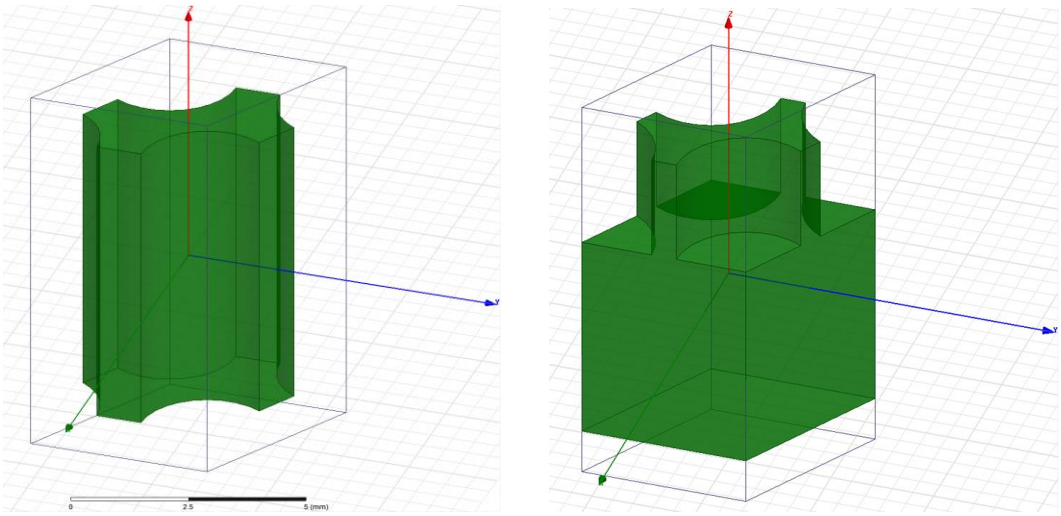

(a) (b)

Fig. 10 (a) Type I unit cell where only the hole diameter is varied and (b) type II unit cell where only the hole depth is varied, the hole diameter is fixed at 3.4mm.

The characteristics of S-parameters, including the phase of S_{12} and magnitude of S_{11} versus hole dimensions are analyzed using finite element method (FEM) of HFSS and results are compared in Fig. 11 and 12. In both Fig. 11 and 12, the curves with different colours represent different angle of incidence ranging from 0^o to 26.6^o by sweeping the position from y = 0 to y = 75 mm with increment of 2 mm. The unit cell is able to generate a phase correction from 0^o to 360^o with either hole diameter varied from 0 to 3.4 mm or hole depth varied from 0 to 7.6 mm. It can be observed that the phase of S_{12} and magnitude of S_{11} for both types of unit cells are not very sensitive toward different angle of incidence.

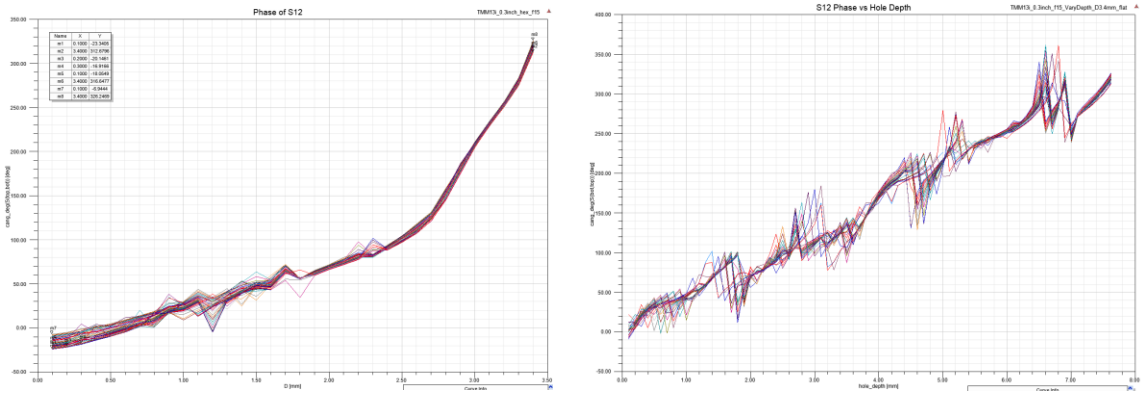

(a) (b)

Fig. 11 Phase of S_{12} (a) versus hole diameter for type I unit cell and (b) versus hole depth for type II unit cell with different angle of incidence.

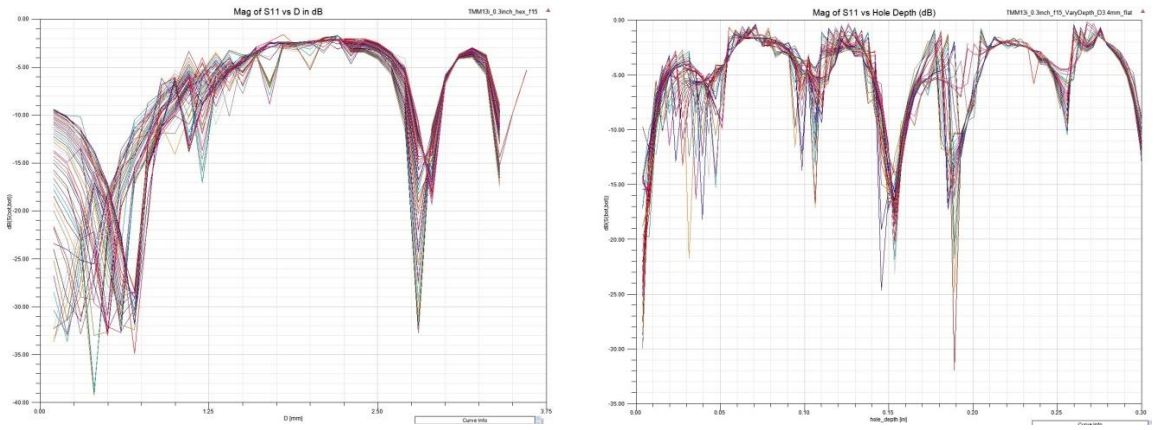

(a) (b)

Fig. 12 Magnitude of S_{11} (a) versus hole diameter for type I unit cell and (b) versus hole depth for type II unit cell with different angle of incidence.

Interestingly, from Fig. 12, the maximum reflections do not occur at the unit cells with smallest hole diameters or depths. In fact, the reflections are very small at the lens center where no holes are drilled there. This makes sense although the effective permittivity there has its maximum of 12.2. Since the thickness of the substrate is 7.62 mm, it is 3.04 times or approximately an integral multiple of the wavelength ($\lambda = \frac{c}{f\sqrt{\varepsilon_r}} \approx$ 2.504 mm) in the TMM13i dielectric medium. We know that from transmission line theory, an integral multiple of a half-wave line transfers the load impedance to the input terminals without change, and air is the load in this case, thus the unit cell is self-matched to the input when there are no holes.

With the given hole diameters in Fig. 12(a) and depths in Fig. 12(b), the amplitudes of reflection coefficients are too high, thus it is recommended that anti-reflection layers to be designed to reduce reflection loss. The effect of anti-reflection layers is discussed later in section 4.1. Also refer to [14], the researchers have applied anti-reflection layers to both the top and bottom of the multilayer dielectric lens, and the reflection coefficient amplitude S_{11} has decreased below −10 dB.

3.3 Lens Design and Simulation Results

Both transmitarray lenses have 20 identical rows of unit cells and cover an area of $15 \times 15 \text{cm}^2$ ($\approx 17.15\lambda_0 \times 17.15\lambda_0$) in x-y plane. The type I lens contains 1366 through holes of various diameters and the type II contains 1210 blind holes with equal diameters. The F/D ratio for both lenses is chosen to be 1, such that a feeding source is placed 15 cm behind the lens.

3.3.1 General Lens Characteristics Comparison

Two types of sources with linear polarization are used to examine the beam collimation capability of each lens. The magnetic Hertzian dipole oriented along x-axis radiates omni-directionally simulates the transmitting mode. The plane wave excitation polarized in y direction can be used to simulate the receiving mode due to reciprocity, where the incoming field from far away is mostly planar. The lenses should convert the planar wave front to omni-directional wave front, and vice versa. Since the lenses have only one dimensional gradient index of refraction along y-axis and they are periodic along x-direction, only the radiation characteristics in the y-z plane are concerned and examined. Thus, to reduce the computational cost, only one slice of each lens across y-z plane (E-plane) is taken for simulation instead of performing the full wave analysis over the entire lens structure. The layouts for type I and type II lenses are shown in Fig. 13 and 14, the lens slices are made periodic along x-direction by applying master and slave boundary conditions on the faces of air-box parallel to y-z plane.

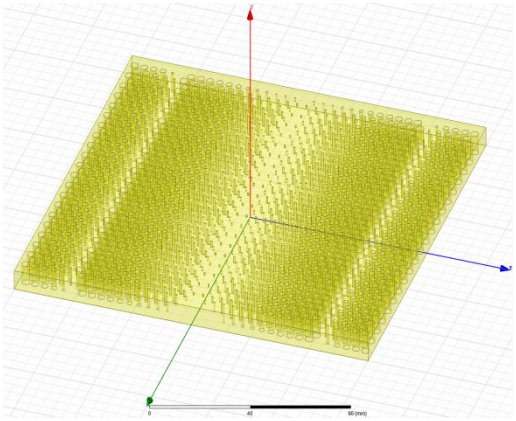

(a)

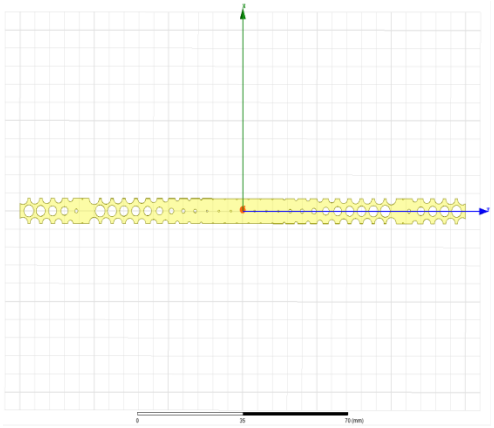

(b)

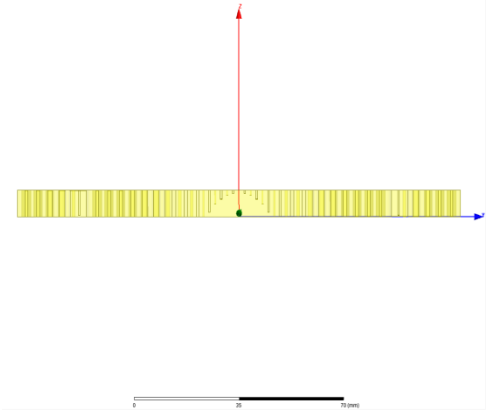

(c)

Fig. 13 (a) Type I lens 3D layout, (b) top view and (c) cross-sectional view of the lens slice.

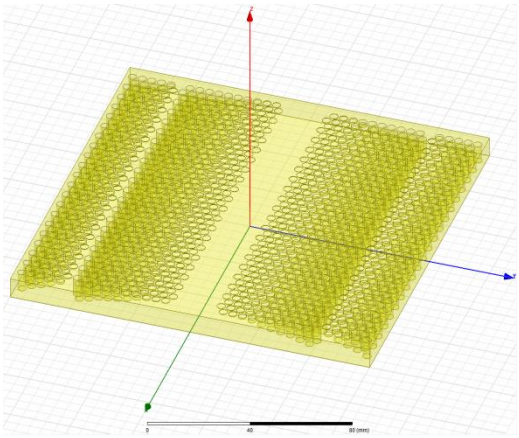

(a)

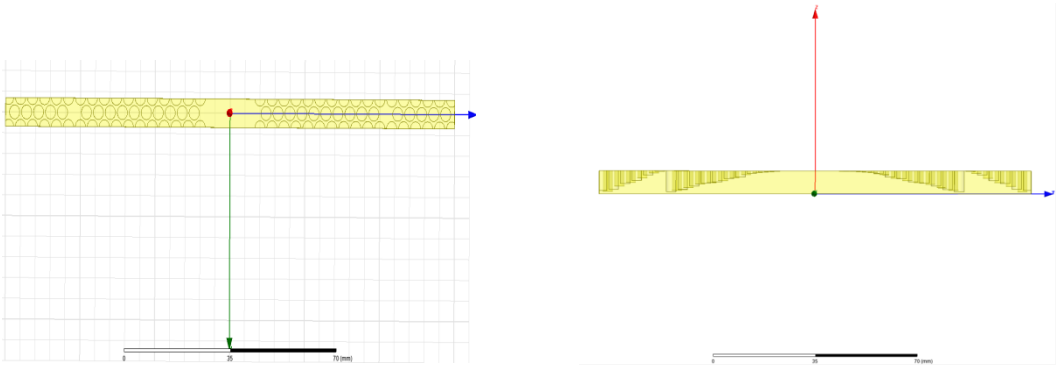

(b) (c)

Fig. 14 (a) Type II lens 3D layout, (b) top view and (c) cross-sectional view of the lens slice.

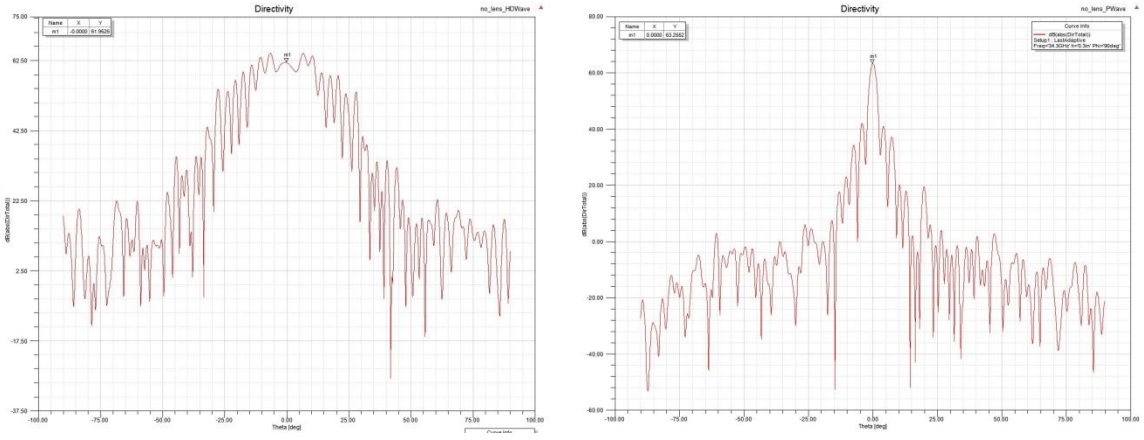

(a) (b)

Fig. 15 Source radiation patterns in E-plane: (a) Infinite magnetic Hertzian dipole and (b) plane wave.

Due to the periodic boundary conditions applied along x, the feeding sources are also repeated infinitely, thus they behave as an infinite-element array along x-direction and the directivities are much larger than a single element. Ideally, the directivities should approach infinity. With lenses removed, the source radiation patterns and directivities in E-plane are simulated and shown in Fig. 15 (a) and (b). The results for both lenses with different sources of excitation are compared and shown in Fig. 16 and 17. The simulation results are also summarized in Table 2. It shows that the Type I lens is about 3 to 4 dB more directive than the Type II lens, and has slightly broader beam width at the design frequency of 34.3GHz. The lower directivity of type II lens is mainly due to the higher reflection at the air to dielectric interface as can also be observed from Fig. 12.

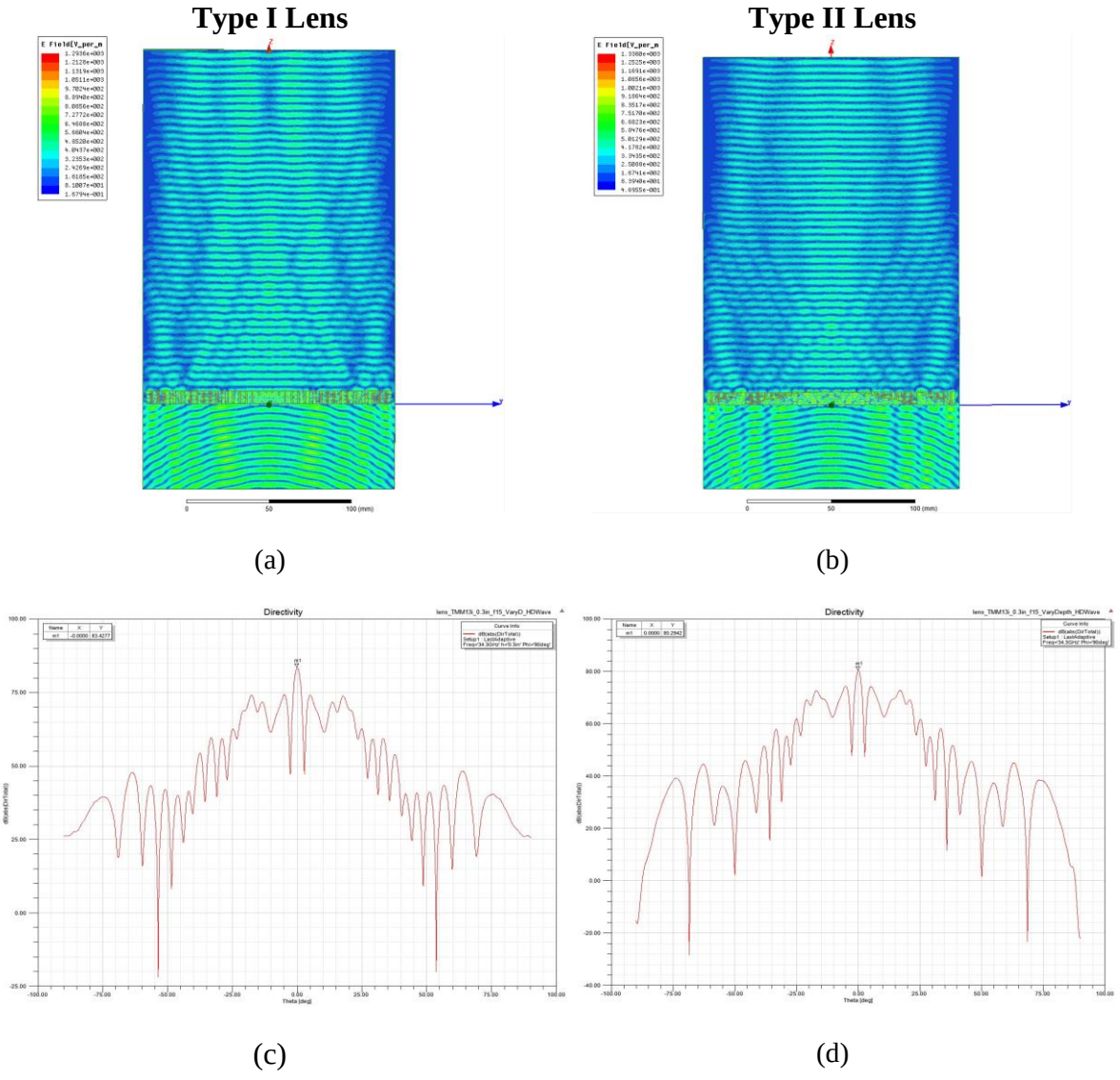

Fig. 16 Infinite magnetic Hertzian dipole excitation of type I lens (left): (a) E-field distribution, (c) radiation pattern and type II lens (right): (b) E-field distribution, (d) radiation pattern.

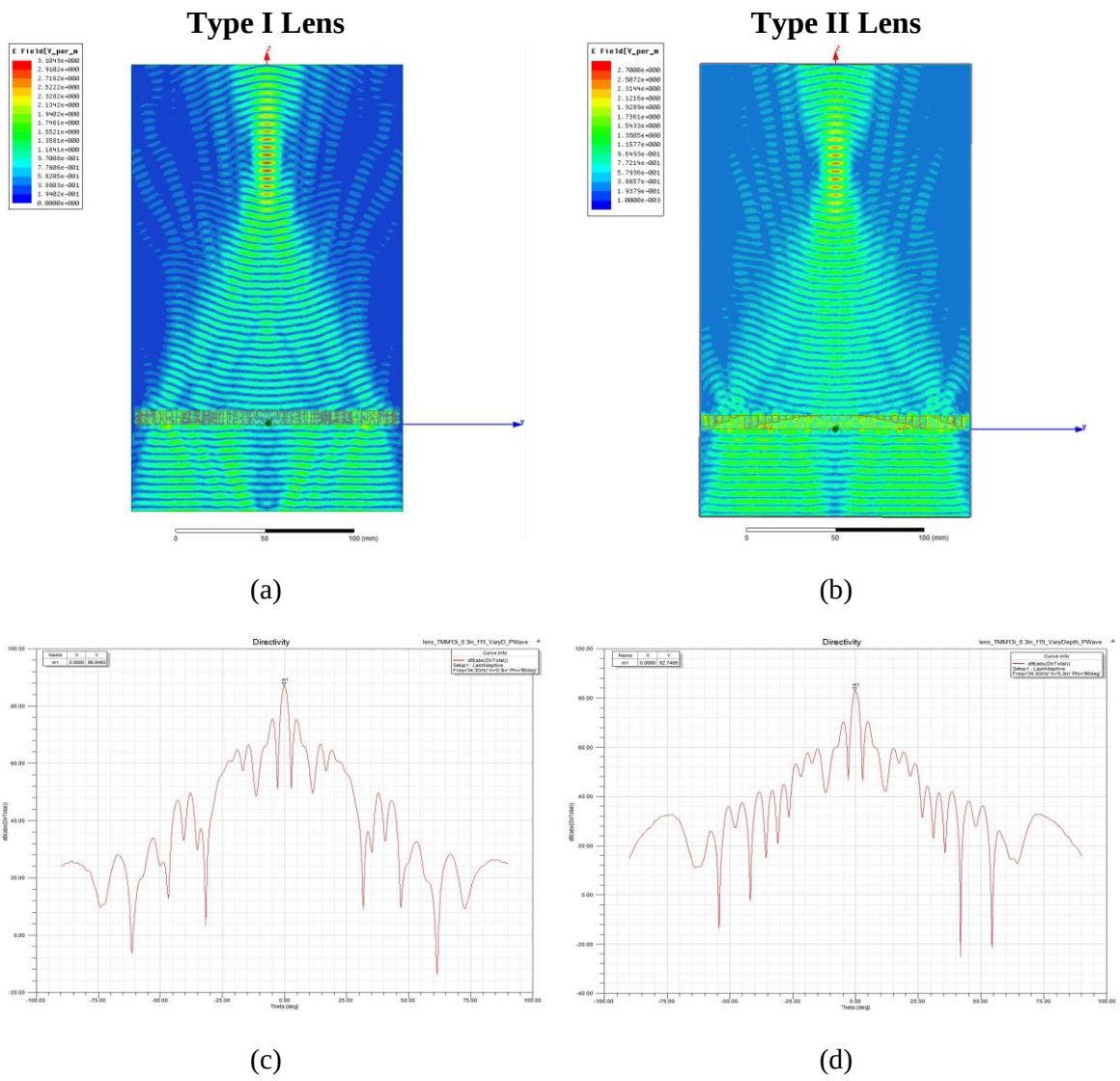

Fig. 17 Plane wave excitation of type I lens (left): (a) E-field distribution, (c) radiation pattern and type II lens (right): (b) E-field distribution, (d) radiation pattern.

Table 2: Summary of radiation characteristics of type I and type II lenses.

Lens Type	**Type I**	**Type II**	**Type I**	**Type II**
Excitation Source	Magnetic Dipole		Plane Wave	
Source Directivity (dB)	61.9		63.3	
Directivity with Lens (dB)	83.4	80.3	86.8	82.7
Directivity Improved (ΔD dB)	21.5	18.4	23.5	19.4
3dB Beamwidth	3.9^{o}	2.54^{o}	2.76^{o}	2.71^{o}
SLL (dB)	74	72.5	75.5	70.1
SLL relative to Max (dB)	-9.4	-7.8	-11.3	-12.6

The directivity improvement is defined as directivity with lens minus the directivity of source.

3.3.2 Beam Scanning Performance

With two types of sources used to feed the transmitarray lenses, different beam scanning mechanisms are investigated accordingly. One technique of beam scanning is achieved by changing the feeding position of the source antenna along y-direction. In this case, the magnetic dipole is used as the source for simulation. In real life, this can be implemented by either mechanically sliding the source antenna along y-direction, or using a switched-beam array as described in [15], where each antenna element can be selected and turned on individually at desired location.

The radiation characteristics for both type I and type II lenses with magnetic Hertzian dipole excitation in E-plane are compared in Fig. 18 and 19 , with position y = 40 mm and 75 mm. The results are also summarized in Table 3 and 4. Note that y = 0 mm is the reference position, where the lenses are center-fed by the source. Both lenses are able to transform the incident omni-directional wave front into planar wave front as feed position changes. As the feed position y is moved to the right, the main lobe directions produced by both lenses are steered leftwards accordingly, and the directivities decrease as the main beams widen and sidelobe levels increase. The sidelobe levels for both lenses are too high and are almost as high as the main lobe when the source is moved to the edge of the lens (y = 75mm). This is not desirable and can cause problem for radar resolving targets. The main reason for high sidelobe levels is due to the broad beamwidth of the source used, and the results can be improved by using sources with narrower beamwidth.

Another way of beam scanning can be achieved by rotating the source antenna (phase center) around a fixed location behind the lens. For this case, the incident plane wave is used as the source. Beam scanning does not have to be limited to mechanical means of course; electronic beam scanning can be achieved if phased array antenna is used as the source instead. By fixing the source at (0, 0, -15cm) or 15cm behind the lens, and modifying the k vector in HFSS, the angle of incidence can be changed. The angle of incidence is expected to be the same as the radiated main lobe direction. The radiation characteristics for both lenses in E-plane are compared in Fig. 20 and Fig. 21, with angle of incidence θ_{inc} = 18.43^o and 26.57^o. The results are also summarized in Table 5 and 6. As θ_{inc}'s for both lenses increase, the main lobes steer away from the normal accordingly, and the directivities decrease as main beams widen and sidelobe levels increase, which are similar to the previous case using magnetic dipole as the source. However, the sidelobe levels are much lower, and they are about 9 dB below the main lobes for both lenses for 26.57^o of incidence. The directivity scan loss is adapted from equation (1) of [16] and can be calculated as:

$$D_{dB}^{scan\ loss} = \left| D_{dB}^{\theta_{scan}=0^o} - D_{dB}^{\theta_{scan}=n^o} \right|, \qquad n^o \in [0^o, \pm 30^o] \tag{8}$$

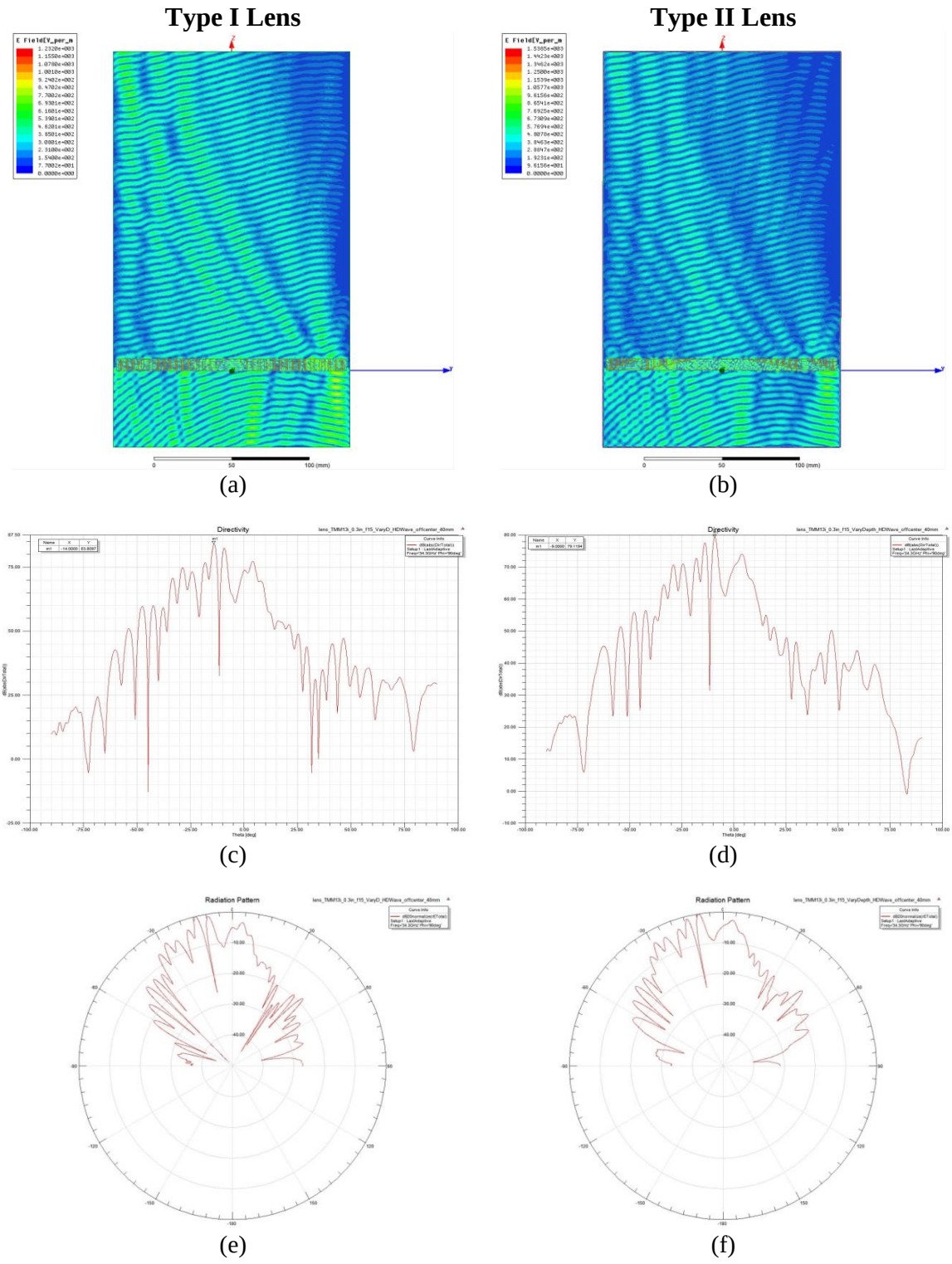

Fig. 18 Magnetic Hertzian dipole excitation of lens at y = 40 mm. Type I (left): (a) E-field distribution, and radiation pattern in (c) rectangular coordinate and (e) polar coordinate. Type II (right): (b) E-field distribution, and radiation pattern in (d) rectangular coordinate and (f) polar coordinate.

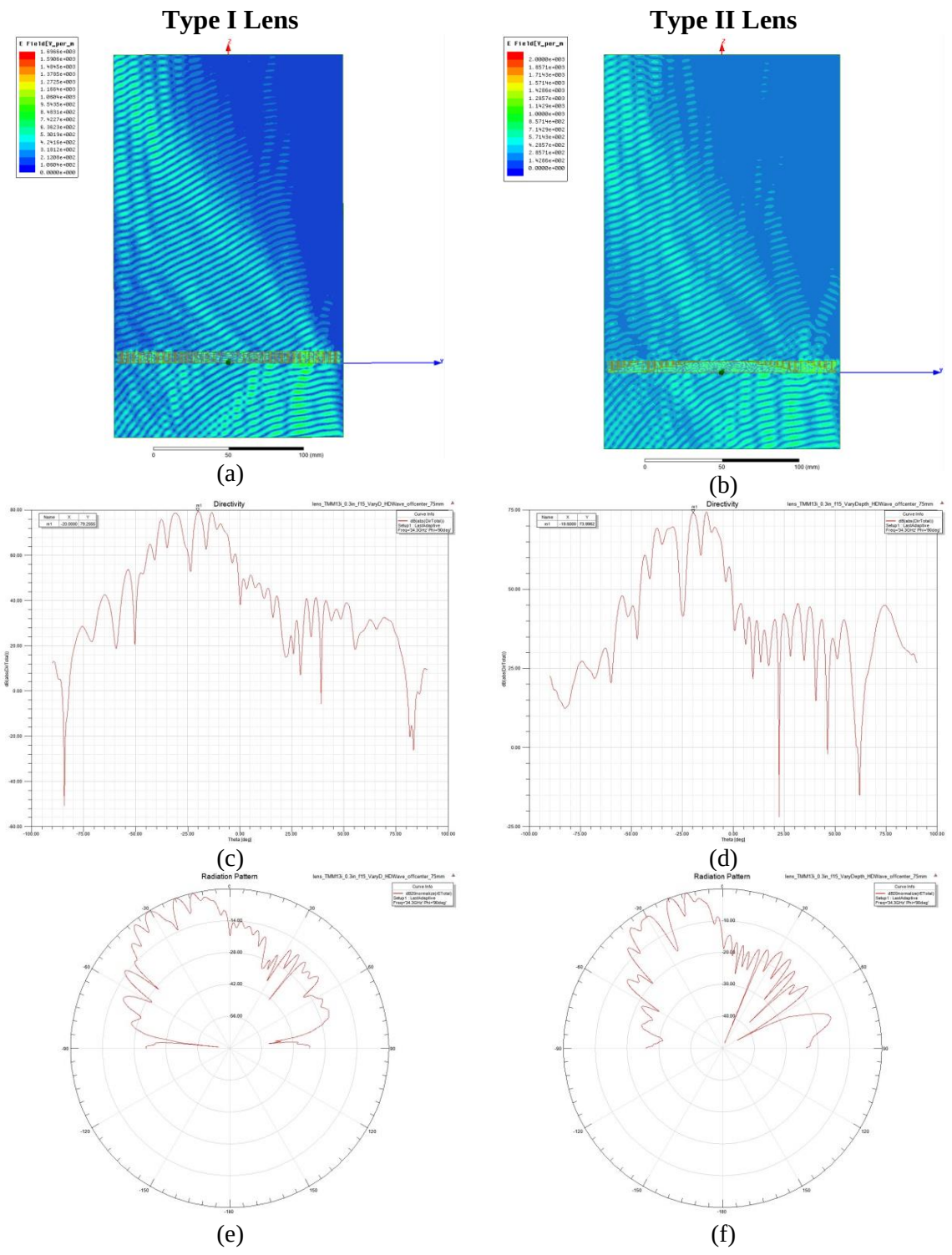

Fig. 19 Magnetic Hertzian dipole excitation of lens at y = 75 mm. Type I (left): (a) E-field distribution, and radiation pattern in (c) rectangular coordinate and (e) polar coordinate. Type II (right): (b) E-field distribution, and radiation pattern in (d) rectangular coordinate and (f) polar coordinate.

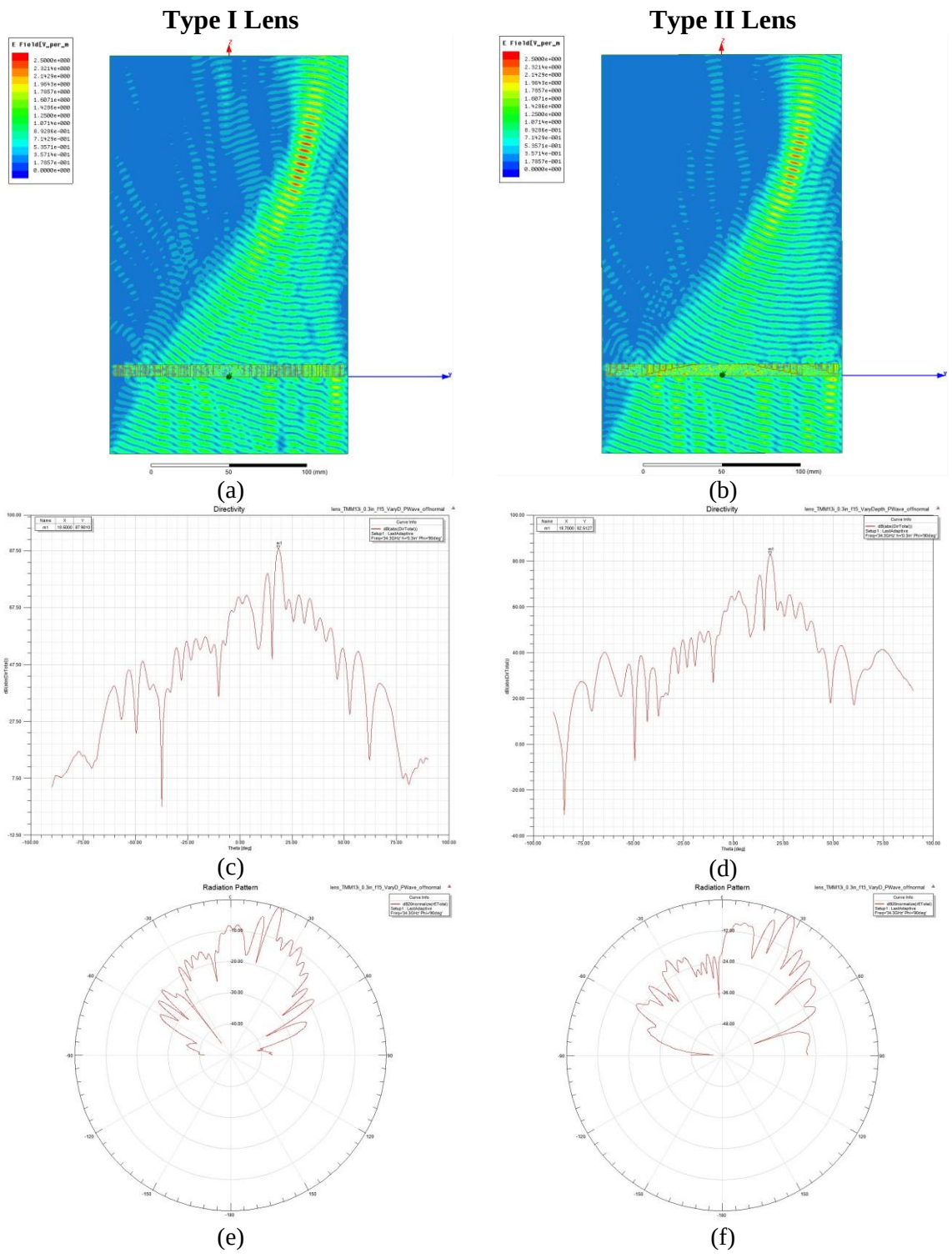

Fig. 20 Plane wave excitation of lens with 18.43^{o} of incidence. Type I (left): (a) E-field distribution, and radiation pattern in (c) rectangular coordinate and (e) polar coordinate. Type II (right): (b) E-field distribution, and radiation pattern in (d) rectangular coordinate and (f) polar coordinate.

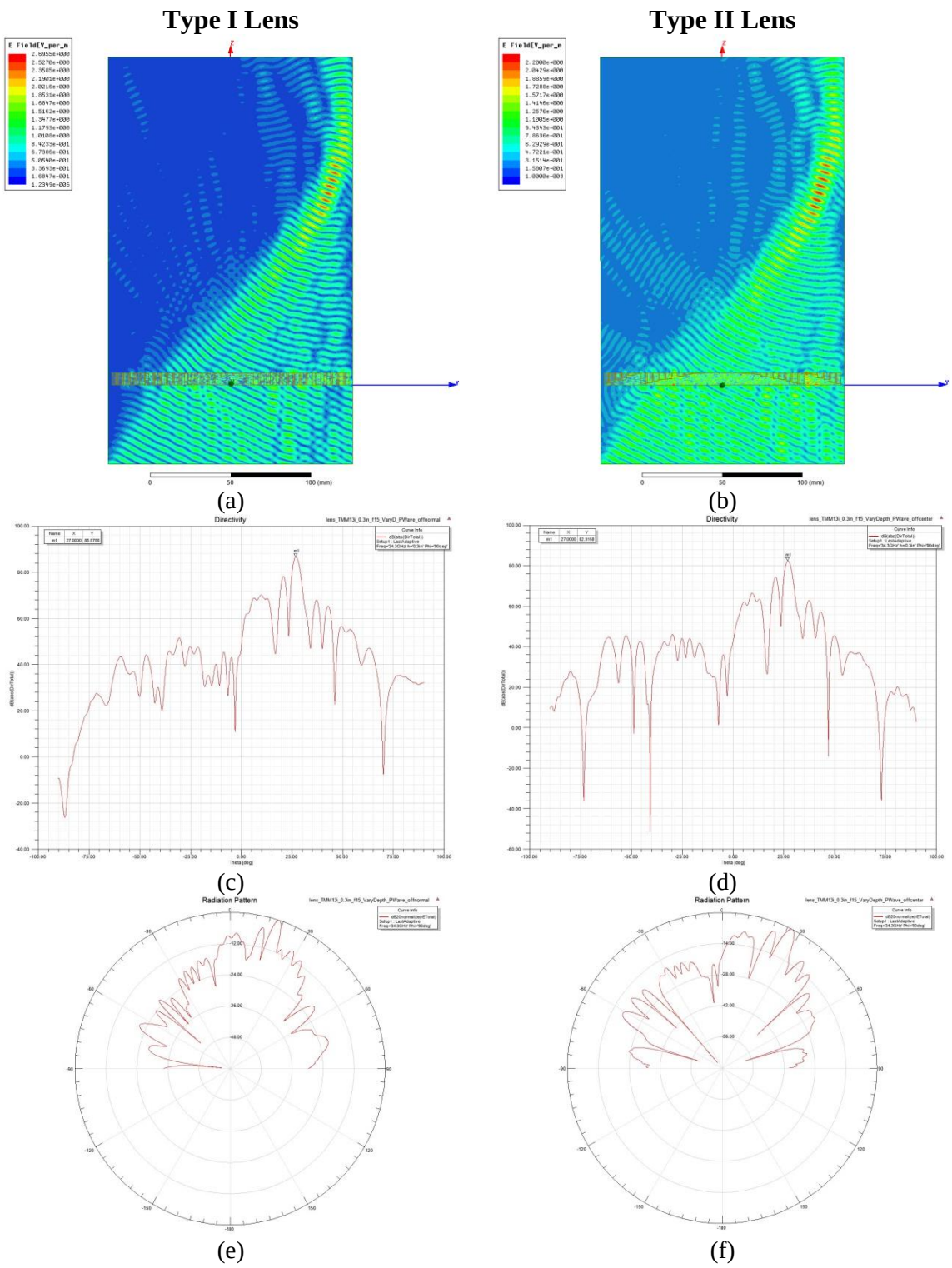

Fig. 21 Plane wave excitation of lens with 26.57^{o} of incidence. Type I (left): (a) E-field distribution, and radiation pattern in (c) rectangular coordinate and (e) polar coordinate. Type II (right): (b) E-field distribution, and radiation pattern in (d) rectangular coordinate and (f) polar coordinate.

Table 3: Summary of radiation characteristics of type I lens with magnetic Hertzian dipole excitation.

y (mm)	Main Beam Direction	Directivity	Directivity relative to Source	3dB Beamwidth	Diectivity Scan Loss
0	0	83.4	21.45	3.9	0
40	-14	83.1	21.15	3.95	0.3
75	-20	79.3	17.35	4.04	4.1

Table 4: Summary of radiation characteristics of type II lens with magnetic Hertzian dipole excitation.

y (mm)	Main Beam Direction	Directivity	Directivity relative to Source	3dB Beamwidth	Directivity Scan Loss
0	0	80.3	18.35	2.54	0
40	-9	79.1	17.15	2.77	1.2
75	-19.5	74	12.05	4.42	6.3

Table 5: Summary of radiation characteristics of type I lens with plane wave excitation.

Incident Angle	Main Beam Direction	Directivity	Directivity relative to Source	3dB Beamwidth	Directivity Scan Loss
0	0	88.8	25.5	2.66	0
18.43	18.5	87.9	24.6	3.12	0.9
26.57	27	86.6	23.3	3.89	2.2

Table 6: Summary of radiation characteristics of type II lens with plane wave excitation.

Incident Angle	Main Beam Direction	Directivity	Directivity relative to Source	3dB Beamwidth	Directivity Scan Loss
0	0	82.7	19.4	2.71	0
18.43	18.6	82.5	19.2	3.16	0.2
26.57	27	82.3	19	3.8	0.4

3.3.3 Frequency Performance

The directivity versus frequency variations for both lens antennas with different excitations are plotted in Fig. 22 and 23. The results are also summarized from Table. 7 to 10.

The frequency performances of type I and type II lenses excited by magnetic dipoles over a frequency range of 6GHz (≈17.5% fractional bandwidth) are compared in Fig. 22. The Type I lens has its local maximum directivity of 89.1dB or 27.2dB relative to the source at 35GHz, which is near the design frequency of 34.3GHz. However, when the frequency moves up to 36GHz, directivities become even higher. This is because the antenna directivity is inversely proportional to the operational wavelength according the relation in (9), thus the effective aperture area of the lens becomes larger at higher

frequencies. Comparing with type I lens, the type II lens has its peak directivity of 80dB, or 20.1dB relative to the source at 34.5GHz. Both lenses have smallest 3dB beamwidth around the design frequency of 34.3GHz, while moving away from the design frequency, beamwidth gradually widens.

$$D = \frac{4\pi}{\lambda_o^2} A_p \tag{9}$$

Bandwidth performance for both lenses can be evaluated from Fig. 22, if we define the 3dB gain bandwidth [17] as where the frequencies at which the directivity has dropped by 3dB of the value at its designed frequency. For type I lens, when frequency moves either down to 33.7GHz or up to 39GHz, the directivity drops about 3dB compare with the directivity at 35GHz, thus, the 3dB fractional bandwidth is about 15%. For type II lens, when frequency moves either down to 34GHz or up to 37.6GHz, the directivity drops about 3dB compare with the directivity at 34.5GHz. The 3dB fractional bandwidth is about 10.5%. The results are also summarized in Table. 7 and 8. A more formal way for bandwidth evaluation is through measuring the magnitude of S_{11} at the feeding port of the source antenna; however, this approach is not available for the current simulation setup, because there is no real antenna used as the source.

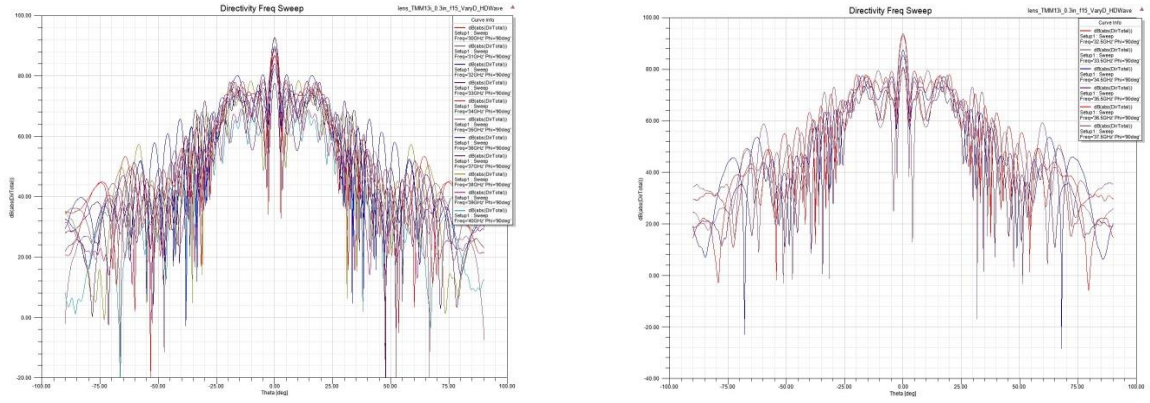

(a) (b)

Fig. 22 Directivity versus frequency for magnetic dipole excitation of (a) type I and (b) type II lenses.

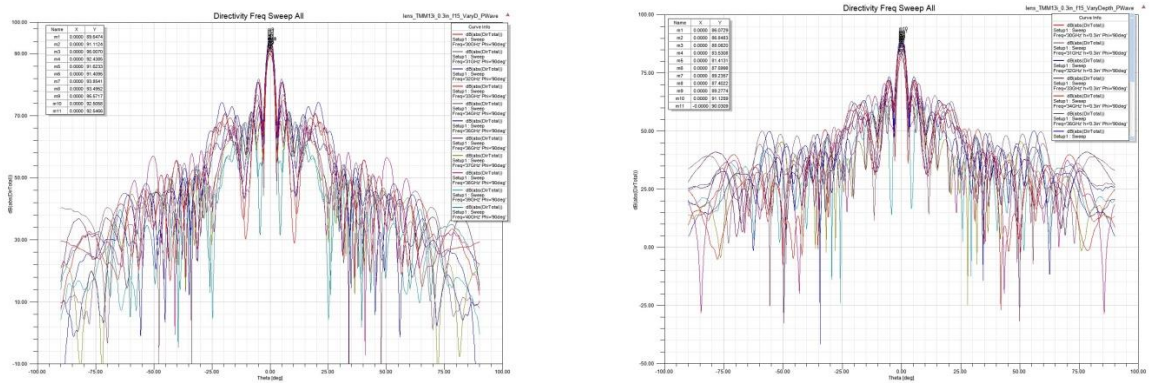

(a) (b)

Fig. 23 Directivity versus frequency for plane wave excitation of (a) type I and (b) type II lenses.

Table 7: Summary of type I lens of magnetic dipole excitation.

Frequency (GHz)	Directivity (dB)	Directivity Relative to Source (dB)	3dB Beamwidth
32	84.1	22.2	2.69°
32.5	80.8	18.9	2.51°
33	79.6	17.7	2.47°
33.5	80.1	18.2	2.46°
34	86.9	25	2.53°
34.5	87.4	25.5	2.63°
35	89.1	27.2	2.7°
35.5	85.4	23.5	2.76°
36	89.7	27.8	2.86°
36.5	91	29.1	2.84°
37	91.7	29.8	2.74°
37.5	91.7	29.8	2.91°
38	91.4	29.5	2.99°
38.5	88.8	26.9	3.22°
39	86.3	24.4	3.44°
40	85.3	23.4	3.88°

Table 8: Summary of type II lens of magnetic dipole excitation.

Frequency (GHz)	Directivity (dB)	Directivity Relative to Source (dB)	3dB Beamwidth
32	72.3	10.4	2.89°
32.5	69	7.1	3.04°
33	70.8	8.9	2.6°
33.5	73.3	11.4	2.64°
34	77.8	15.9	2.61°
34.5	82	20.1	2.65°
35	81	19.1	2.7°
35.5	80.1	18.2	2.8°
36	77.5	15.6	2.86°
36.5	77.4	15.5	2.77°
37	80.4	18.5	2.82°
37.5	79.8	17.9	2.9°
38	78.4	16.5	3.02°

Similar results for plane wave excitation for both lenses are summarized in Table. 9 and 10, and the directivity versus frequency relations are also plotted in Fig. 23 for comparison. The directivity variations for plane wave excitation are much smaller than magnetic dipole excitations.

Table 9: Summary of type I lens of plane wave excitation.

Frequency (GHz)	Directivity (dB)	Directivity Relative to Source (dB)	3dB Beamwidth
30	89.6	26.3	3.38
31	91.1	27.8	3.22
32	91	27.7	3.06
33	91.4	28.1	2.78
34	91.6	28.3	2.64
35	91.4	28.1	2.82
36	92.8	29.5	2.88
37	93.5	30.2	2.8
38	95.6	32.3	2.86
39	92.5	29.2	2.96
40	92.5	29.2	3.04

Table 10: Summary of type II lens of plane wave excitation.

Frequency (GHz)	Directivity (dB)	Directivity Relative to Source (dB)	3dB Beamwidth
30	86.1	22.8	3.4^o
31	86.8	23.5	3.22^o
32	87.1	23.8	3^o
33	87.5	24.2	2.82^o
34	88.4	25.1	2.62^o
35	87.6	24.3	2.82^o
36	89.2	25.9	2.86^o
37	87.4	24.1	2.84^o
38	89.3	26	2.8^o
39	91.1	27.8	2.9^o
40	90	26.7	2.98^o

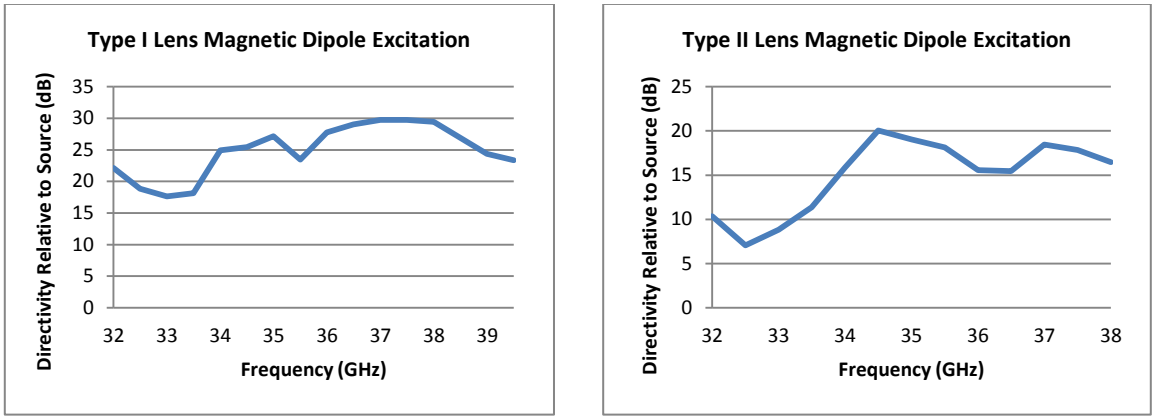

(a) (b)

Fig. 22 Directivity versus frequency for magnetic dipole excitation of (a) type I and (b) type II lenses.

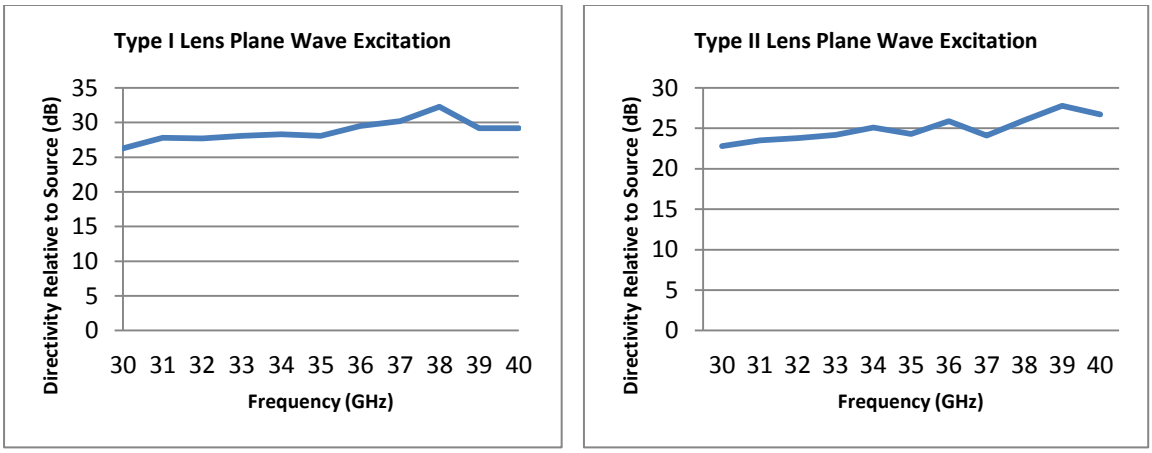

(a) (b)

Fig. 23 Directivity versus frequency for plane wave excitation of (a) type I and (b) type II lenses.

4. Future Works and Discussions

Aperture efficiency is a measure of how well we can use the lens. There are mainly three types of losses that contribute to the reduction of aperture efficiency in this design; they are reflection loss, spillover loss and illumination loss. The aperture efficiency can be improved by properly adjusting the F/D ratio of the lens and adding a layer or multi-layer of anti-reflective coating to the lens surface.

4.1 Design of Anti-reflective Layer

Due to the large contrast between the refractive indices of air and TMM13i substrate, an anti-reflective layer has been considered to reduce the reflection. Anti-reflective coatings have been widely used on eye glasses and many other optical devices. Other well-known examples of anti-reflective coatings or layers include moths' eyes with surfaces covered with a natural nanostructured film, and pyramidal radiation absorbent materials on the walls of anechoic chambers to mimic free-space environment.

A well designed anti-reflective layer does not only reduce the reflection loss, but also maintains phase uniformity through the layer across entire lens surface. Although the anti-reflective structure is yet to be fully implemented, some promising results are demonstrated through the simulation of unit cells at different locations on the lens surface. The design method is adapted from optical science, with combination of impedance matching and effective medium theory. Consider the case of normal incidence and use Fresnel equation, the intensity of electromagnetic wave reflected from the lens is given by the reflectance *R*:

$$R = \left(\frac{n_0 - n_s}{n_0 - n_s}\right)^2 \tag{10}$$

where n_0 and n_s are the refractive indices of the air and the substrate material respectively. With another thin layer added between the air and the substrate, the electromagnetic wave now reflects twice: once from the interface between air and the thin layer, and once from the interface between the thin layer and the substrate. To minimize reflection, the thin layer has to satisfy two conditions [18] such that:

1) $n_{AR} = \sqrt{n_0 n_s}$, such that intensity of the two reflected waves have the same amplitude, where n_{AR} is the refractive index of the anti-reflective layer. In terms or relative permittivity:

$$\varepsilon_{r,\,AR} = \sqrt{\varepsilon_{r,0}\varepsilon_{r,s}} \tag{11}$$

2) Two reflected waves are 180^o out of phase, or of destructive interference. It requires the electrical thickness of the anti-reflective layer to be $n_{AR}\,h_{AR} = (2m+1)\frac{\lambda_0}{4}$, where λ is the free space wavelength. Thus, the minimum required thickness of coating is:

$$h_{AR} = \frac{\lambda_{AR}}{4} = \frac{\lambda_0}{4\sqrt{\varepsilon_{r,AR}}} \tag{12}$$

where λ_{AR} and λ_0 are the wavelengths in the layer and in the air respectively. The mechanism is shown in the following figure []:

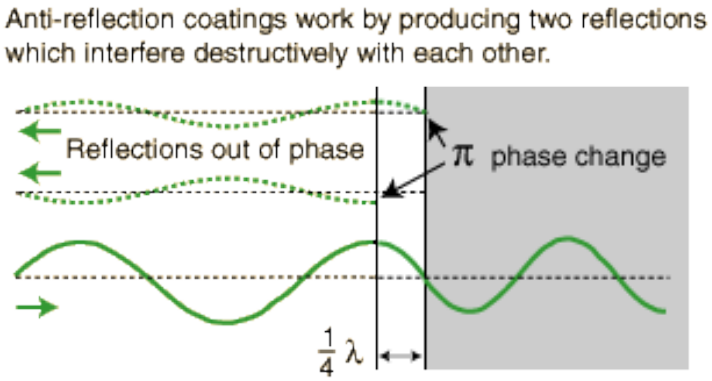

Fig.24 Interference in a quarter-wave anti-reflection coating.

For simplicity, only a single layer of anti-reflective coating is applied to the bottom of type II lens to match the air and substrate interface. Using equation (11) and (12) from above, the relative permittivity $\varepsilon_{r,AR}$ is found to be about 3.5 and the thickness of the layer is about 1.2 mm. Materials with relative permittivity exactly the same as $\varepsilon_{r,AR}$ are not easily found, however with effective medium theory stated in [13], the required effective dielectric constant can be achieved through perforation of the matching layer. The material chosen for perforation is Rogers RO3006, a PTFE based material with dielectric constant 6.15 and loss tangent 0.0025. Derived from equation (2), the required hole diameter for anti-reflective layer can be approximated using:

$$d_{AR} = s \cdot \sqrt{\frac{2\sqrt{3}}{\pi} \frac{6.15 - \varepsilon_{eff,AR}}{6.15 - 1}} \tag{13}$$

with hole spacing s = 4mm, the hole diameter d_{AR} is calculated to be 3 mm. The RO3006 substrate is chosen because it has bondply as its own material [10], so there is no need to introduce a different material to bond the anti-reflective layer to the surface of the lens, it reduces multi-reflections and makes adhesion stronger between different materials. The unit cell model is demonstrated in Fig. 28, where the anti-reflective coating is in yellow.

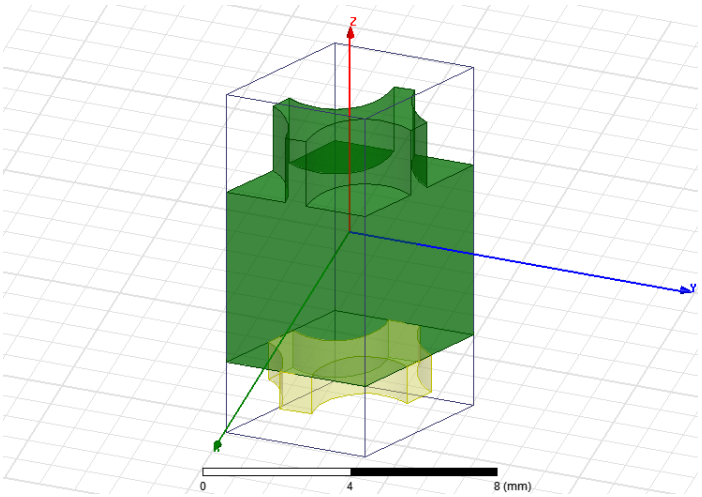

Fig. 28 Unit cell model with anti-reflective coating.

Notice that the above analysis only considers normal incidence where $\theta_{inc} = 0^o$ and it only works well near the center of the lens. Refer back to Fig. 4, when the incidence is oblique, or away from the lens center, the electrical thickness of the single layer of coating becomes $n_{AR} h_{AR} \cos \theta_{inc}$. Since h_{AR} is fixed to make the lens flat, and cos θ_{inc} decreases as the angle of incidence θ_{inc} increases, n_{AR} needs to be adjusted accordingly to ensure the electrical length of the layer stays constant and equalizes the phase delay. The refractive index n_{AR}, or equivalently, the effective permittivity $\varepsilon_{eff,AR}$ has to increase as the incidence moves away from normal. This is also evident in Fig. 29(b), which shows the phase shift versus hole diameters with respect to different angles of incidence for the anti-reflective layer. Each curve represents each angle of incidence, if we draw a equi-phase line (shown in blue) intercepting all the curves, and read off the horizontal coordinates of the intercepts, we can observe that indeed the hole diameters, or equivalently the effective permittivity have to decrease as θ_{inc} increases. For phase equalization, it has to satisfy the following relationship at all locations on the lens surface, such that:

$$\Phi_{AR} = \Phi_{lens\ with\ AR}(y) - \Phi_{lens\ without\ AR}(y) = Const. \qquad \forall\ y \tag{14}$$

where Φ_{AR}, $\Phi_{lens\ with\ AR}$, and $\Phi_{lens\ without\ AR}$ are the phase delays through the anti-reflective layer, lens with anti-reflective layer and lens without anti-reflective layer respectively. And y can be any location on the lens.

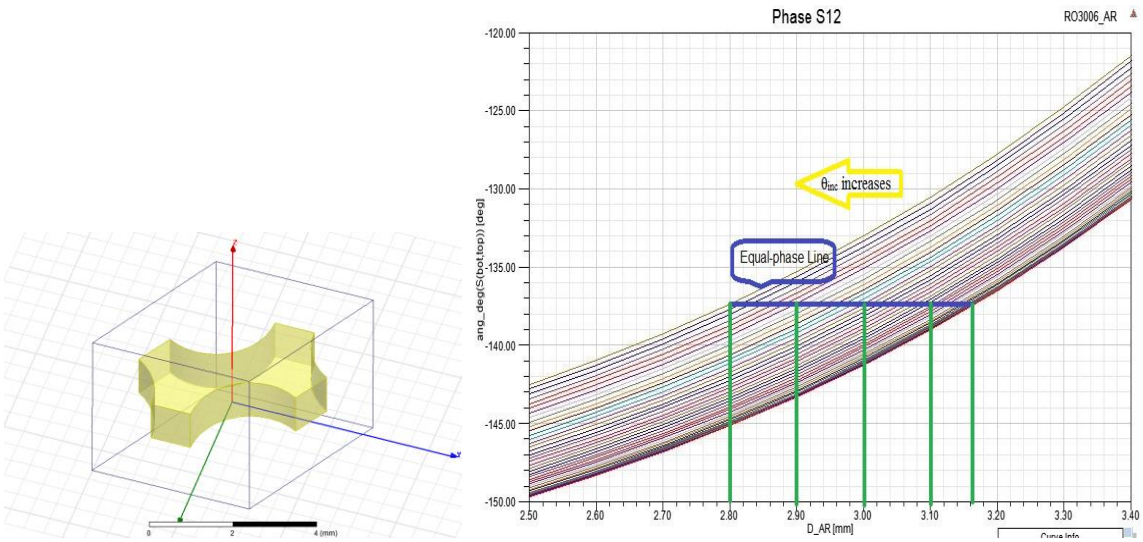

Fig. 29 (a) Unit cell of the anti-reflective layer and (b) phase of S_{12} versus hole diameter with respect to different angles of incidence of the unit cell.

Since phase is more sensitive toward the variation of hole diameters than the reflection coefficient, phase equalization through the anti-reflective layer has to be the primary design consideration, such that lens focusing capability will not be distorted. By drawing an equi-phase line at -137.5^{o} across all curves in Fig. 29(b), the hole diameter variation d_{AR} can be restricted in the vicinity of 3mm, or between 2.8 to 3.2mm. The required hole diameters at each location on the lens can be determined by reading off the values on the horizontal axis (the green vertical lines). Although those hole diameters do not always provide the best impedance match, reflection is still reduced since it satisfies that $n_0 < n_{AR} < n_s$. Choosing the unit cells at y = 26mm, 32mm, 62mm and 72mm, which have the strongest reflection, the S_{11}'s versus frequency from 30 to 40GHz with and without anti-reflective layers are plotted as from Fig. 30 to 33. The results are also summarized in the following table.

Table 10: Summary of effects of adding anti-reflective layer at selected locations on the lens.

	No AR		**With AR**			
Location y	**$\|S_{11}\|$ (dB)**	**arg(S_{12})**	**$\|S_{11}\|$ (dB)**	**arg(S_{12})**	**Reflection Reduced (dB)**	**Phase Delay by AR**
26mm	-1.88	28.96^{o}	-17.53	-27.73^{o}	15.65	56.69^{o}
32mm	-2.35	70.91^{o}	-5.85	37.66^{o}	3.5	33.25^{o}
62mm	-2.22	79.22^{o}	-6.91	34.23^{o}	4.69	44.99^{o}
72mm	-2.72	-116.63^{o}	-8.77	-171.22^{o}	6.05	54.59^{o}

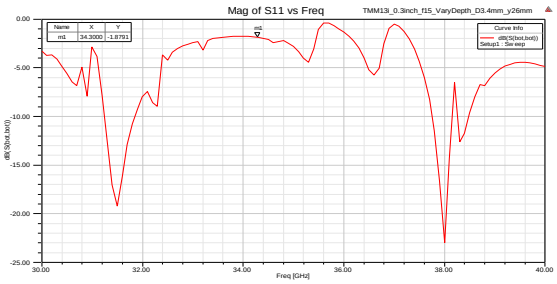

(a)

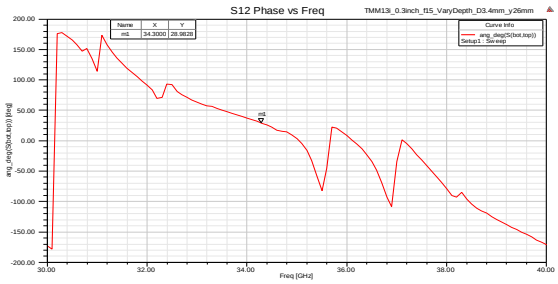

(b)

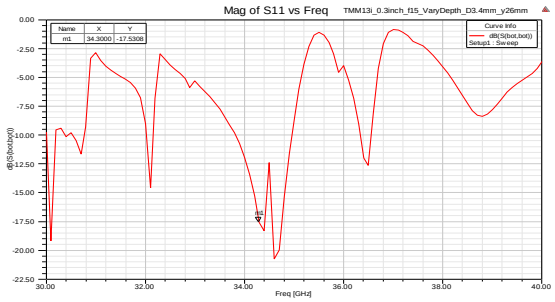

(c)

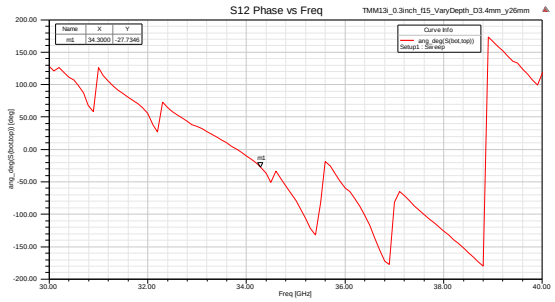

(d)

Fig. 30 (a) Magnitude of S_{11} in dB and (b) Phase of S_{12} without anti-reflective layer, and (a) Magnitude of S_{11} in dB and (b) Phase of S_{12} with anti-reflective layer at y = 26mm.

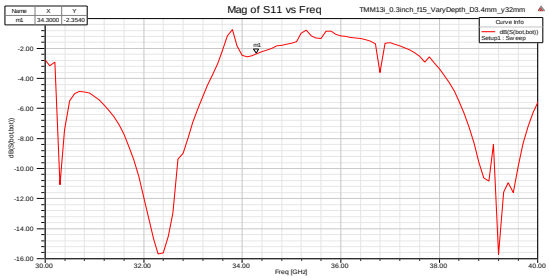

(a)

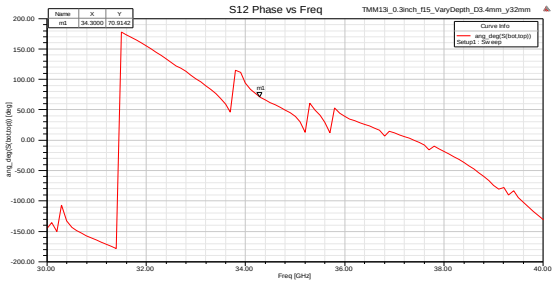

(b)

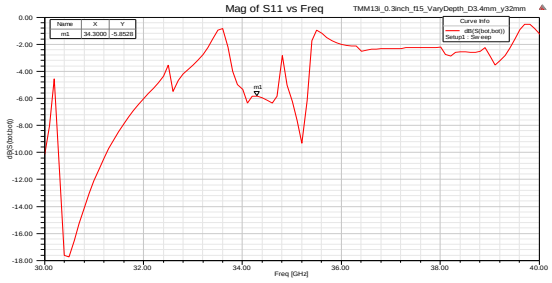

(c)

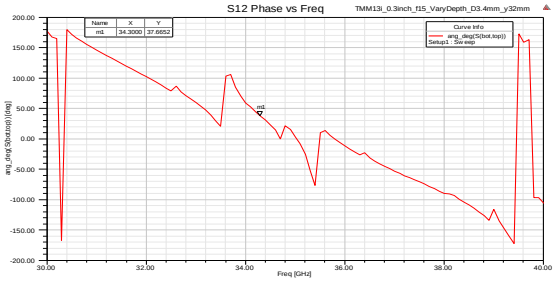

(d)

Fig. 31 (a) Magnitude of S_{11} in dB and (b) Phase of S_{12} without anti-reflective layer, and (a) Magnitude of S_{11} in dB and (b) Phase of S_{12} with anti-reflective layer at y = 32mm.

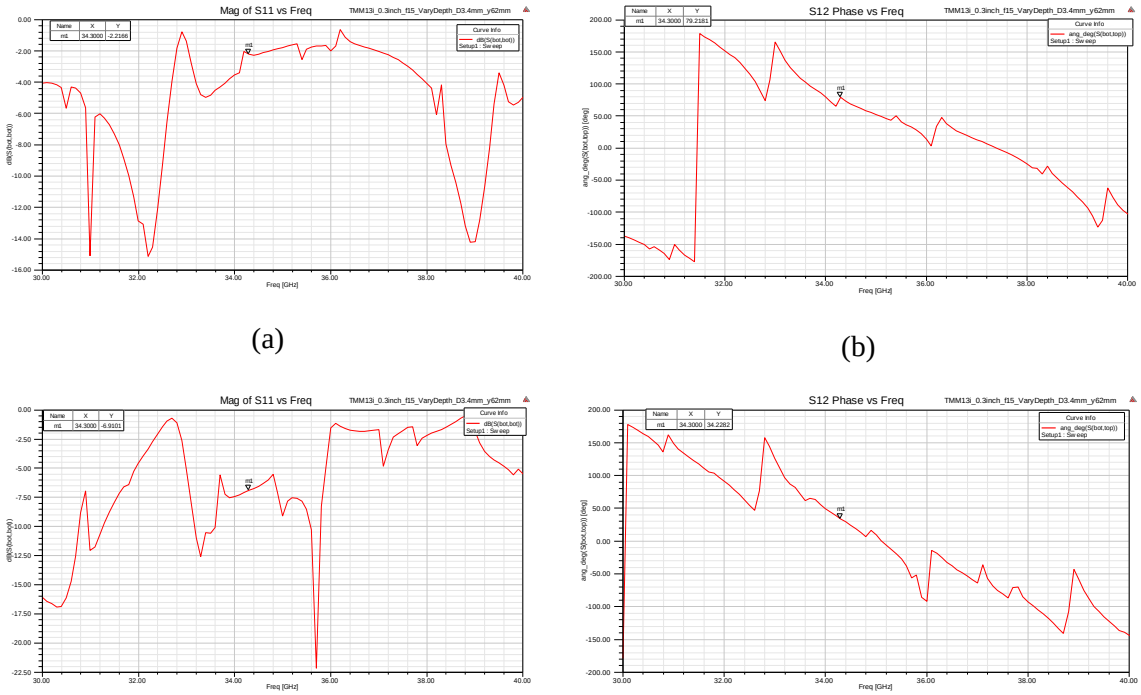

Fig. 32 (a) Magnitude of S_{11} in dB and (b) Phase of S_{12} without anti-reflective layer, and (a) Magnitude of S_{11} in dB and (b) Phase of S_{12} with anti-reflective layer at y = 62mm.

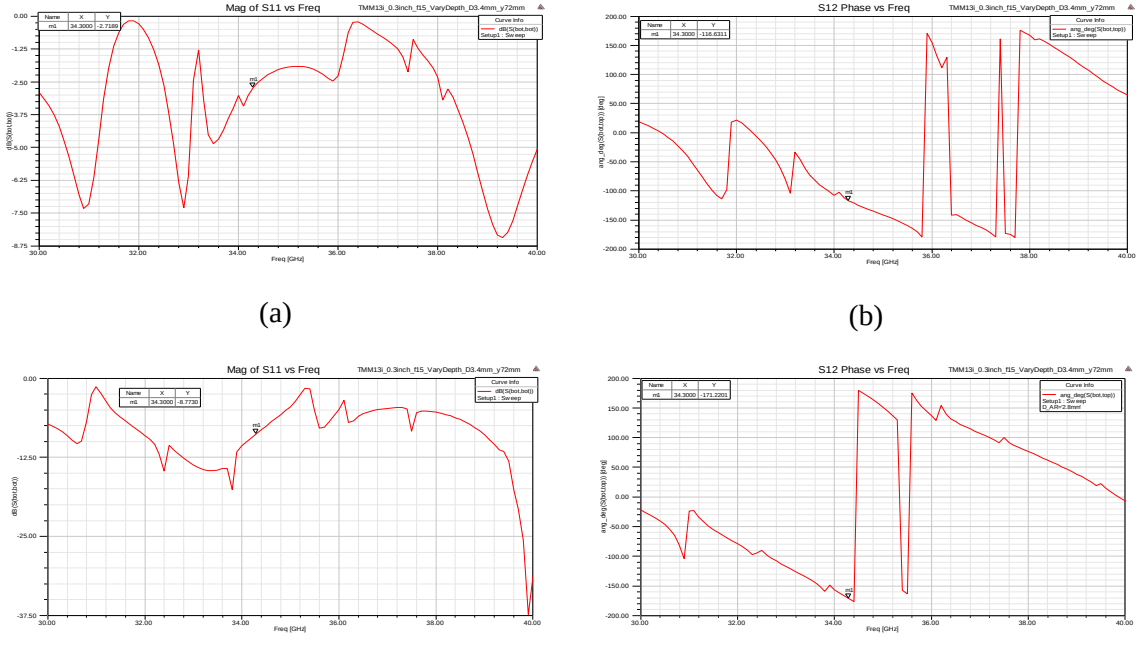

Fig. 33 (a) Magnitude of S_{11} in dB and (b) Phase of S_{12} without anti-reflective layer, and (a) Magnitude of S_{11} in dB and (b) Phase of S_{12} with anti-reflective layer at y = 72mm.

4.2 F/D Ratio Optimization

The illumination mechanism of the transmitarray lens antenna is similar to a reflector antenna, except reflector antennas usually employ a curved surface. Lens aperture efficiency depends on both the radiation pattern of the feed antenna and the F/D ratio. When the feed antenna illuminates the lens, most of the radiated power is intercepted and collimated by the lens, but there is always some part of energy misses the lens; this loss is known as spillover. Ideally, all areas of the lens should be illuminated uniformly with equal power and in phase from the feed. However, since the edges of the lens are farther away from the focus than the center of the lens, more power will be required at the edges than the center, but with no power missing the lens. This ideal radiation pattern is not realizable by any real feed antennas, and it always tapers toward the edge as shown in Fig. 34, thus perfectly uniform illumination cannot be achieved. Fig. 34 below shows the idealized radiation pattern versus a typical feed radiation pattern; the difference between the idealized feed pattern and the actual feed pattern results in illumination loss (as coloured in blue) because some areas of the lens are unable to work as effectively as the others [20].

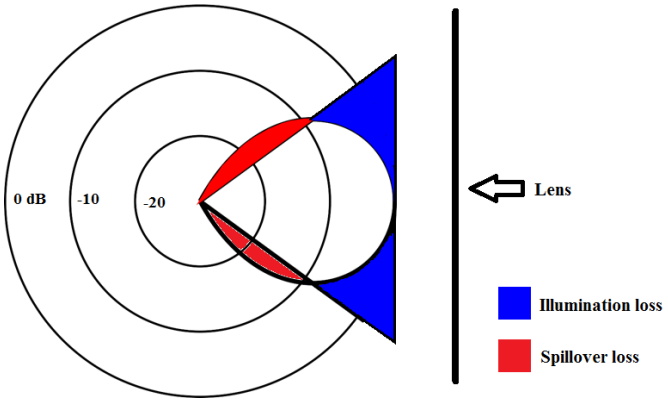

Fig. 34 Typical versus desired lens illumination

For a lens antenna with given feed radiation pattern, there is always a trade-off between the spillover and taper efficiencies, an optimal F/D ratio has to be chosen to achieve maximum aperture efficiency. As the feed moves away from the aperture, the source wave front is more planar, thus aperture becomes more uniformly illuminated and taper efficiency is increased. However, spillover efficiency is decreased as more power spills outside the aperture. The compromise between are demonstrated in Fig. 35, large F/D ratio gives good taper efficiency but poor spillover efficiency, and vice versa [21]. Similar relationship is also reported in [22] with result shown in Fig. 36, where for a microstrip reflectarray antenna fed by a source with $cos^q\ \theta$ pattern, the optimal efficiency is achieved for F/D ratio between 0.7 and 1.

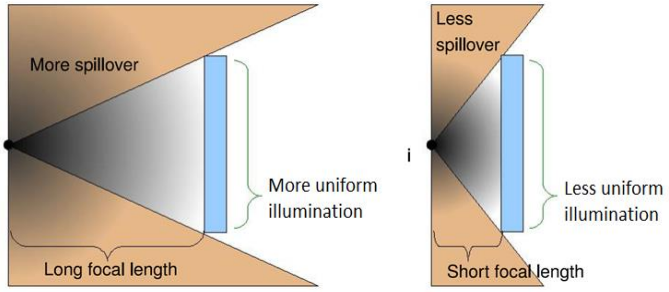

Fig. 35 Trade-off between the illumination and spillover efficiencies. The thin rectangle represents the lens whereas the triangles show the angular extent of the spillover [21].

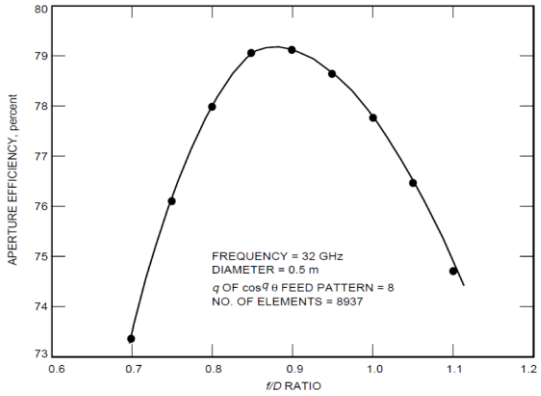

Fig. 36 Microstrip reflectarray aperture efficiency versus f/D ratio from [22].

The choice of feed will also influence the transmitarray lens antenna's aperture efficiency. A rule of thumb commonly used for parabolic dish design may also be adopted for transmitarry lens design, such that the feed should be designed for a radiation pattern which is 10dB down at the edge of the aperture for optimal aperture efficiency [20].

5. Conclusion

Transmitarray lenses with two different perforation schemes were presented. Both lenses were designed using a single layer of 3 inch thick TMM13i substrate. The phase compensation for the transmitted signal is controlled by either varying the hole diameters or depths to achieve required dielectric constant at different locations on the lens. Both lenses are able to provide 360^{o} phase compensation with high directivity and narrow beamwidth. However, anti-reflective layers should be apply to the lens surface to reduce reflection loss. Lens aperture efficiency can also be optimized by adjusting the F/D ratio.

References

1. D. L. Sengupta and T. K. Sarkar, “Microwave and Millimeter Wave Research before 1900 and the Centenary of the Horn Antenna,” Microwave Conference, 1995. 25th European, Vol. 2, pp. 903–909, 1995.
2. J. Y. Lau and S. V. Hum, "A Planar Reconfigurable Aperture With Lens and Reflectarray Modes of Operation," in IEEE Transactions on Microwave Theory and Techniques, vol. 58, no. 12, pp. 3547-3555, Dec. 2010.
3. Ryan, C. G. M., M. R. Chaharmir, J. Shaker, J. R. Bray, Y. M. M. Antar, and A. Ittipiboon, “A wideband transmitarray using dual-resonant double square rings,” IEEE Trans. Antennas Propagat., Vol. 58, No. 5, 1486–1493, May 2010.
4. Ryan, C. G. M., J. R. Bray, Y. M. M. Antar, M. R. Chaharmir, J. Shaker, and A. Ittipiboon, “A broadband transmitarray using double square ring elements,” 13th International Symposium on Antenna Technology and Applied Electromagnetics and the Canadian Radio Sciences Meeting, ANTEM/URSI 2009, Toronto, 2009.
5. A. A. Awaleh, S. H. Dahlan and M. Z. M. Jenu, "A compact flat lens antenna with aperture coupled patch elements," Applied Electromagnetics (APACE), 2014 IEEE Asia-Pacific Conference on, Johor Bahru, 2014, pp. 23-26.
6. D. N. Black and J. C. Wiltse, "Millimeter-Wave Characteristics of Phase-Correcting Fresnel Zone Plates," in IEEE Transactions on Microwave Theory and Techniques, vol. 35, no. 12, pp. 1122-1129, Dec 1987.
7. Y. Zhang, R. Mittra and W. Hong, "A zoned two-layer flat lens design," Antenna Technology (iWAT), 2011 International Workshop on, Hong Kong, 2011, pp. 412-415.
8. M. K. T. Al-Nuaimi and W. Hong, "Analysis and design of inhomogeneous single layer slotted dielectric flat lens," Antennas & Propagation (ISAP), 2013 Proceedings of the International Symposium on, Nanjing, 2013, pp. 480-483.
9. M. K. T. Al-Nuaimi, W. Hong and Y. Zhang, "Design of High-Directivity Compact-Size Conical Horn Lens Antenna," in IEEE Antennas and Wireless Propagation Letters, vol. 13, no. , pp. 467-470, 2014.
10. Rogers Product Selector Guide, https://www.rogerscorp.com/documents/2532/acs/ACS-Product-Selector-Guide-and-Standard-Thicknesses-and-Tolerances.pdf
11. J. Thornton, K. C. Huang, “Modern Lens Antennas for Communications Engineering”, Wiley-IEEE Press, pp. 117, April 2013
12. Rogers Proprietary & Confidential, Technical Report No. 6029, Dielectric Constant Anisotropy of RO3010®, RO3006®, RT/duroid® 6010LM, and RT/duroid® 6006 Laminates

13. A. Petosa and A. Ittipiboon, "Design and performance of a perforated dielectric fresnel lens," in IEE Proceedings - Microwaves, Antennas and Propagation, vol. 150, no. 5, pp. 309-314, 10 Oct. 2003.
14. A. E. Mahmoud, W. Hong, Y. Zhang and A. Kishk, "W-Band Mutlilayer Perforated Dielectric Substrate Lens," in IEEE Antennas and Wireless Propagation Letters, vol. 13, no. , pp. 734-737, 2014.
15. M. Imbert, J. Romeu and L. Jofre, "Design of a dielectric flat lens antenna for 60 GHz WPAN applications," Antennas and Propagation Society International Symposium (APSURSI), 2013 IEEE, Orlando, FL, 2013, pp. 1164-1165.
16. M. K. T. Al-Nuaimi and Wei Hong, "On the beam scanning capabilities of discrete dielectric flat lens at 73.5GHz and 83.5GHz," Wireless Symposium (IWS), 2015 IEEE International, Shenzhen, 2015, pp. 1-4.
17. R. Yang, Z. Lei, L. Chen, Z. Wang and Y. Hao, "Surface Wave Transformation Lens Antennas," in IEEE Transactions on Antennas and Propagation, vol. 62, no. 2, pp. 973-977, Feb. 2014.
18. Q.Tian, Y. B. Liao and L. Q. Sun, “Engineering Optics”, Tsinghua University Press, pp. 220, 1991.
19. “Anti-Reflection Coatings”, HyperPhysics, http://hyperphysics.phy-astr.gsu.edu/hbase/phyopt/antiref.html
20. P. Wade, “Parabolic Dish Feeds - Performance Analysis”, pp. 1, March 1998.
21. R. H. Phillion, “Flat lenses for circularly polarized electromagnetic waves,” Ph.D dissertation, University of Calgary, 2010.
22. J. Huang, “Analysis of a Microstrip Reflectarray Antenna for Microspacecraft Applications,” Jet Propulsion Laboratory, 1995, TDA Progress Rep. 42-120.